

THE DOUBLE PEAKED SN 2013ge: A TYPE Ib/c SN WITH AN EARLY ASYMMETRIC MASS EJECTION OR AN EXTENDED PROGENITOR ENVELOPE

M. R. DROUT¹, D. MILISAVLJEVIC¹, J. PARRENT¹, R. MARGUTTI¹, A. KAMBLE¹, A. M. SODERBERG¹, P. CHALLIS¹, R. CHORNOCK², W. FONG^{3,4}, S. FRANK⁵, N. GEHRELS⁶, M. L. GRAHAM⁷, E. HSIAO^{8,9}, K. ITAGAKI¹⁰, M. KASLIWAL¹¹, R. P. KIRSHNER¹, D. MACOMB¹², G. H. MARION¹³, J. NORRIS¹², M. M. PHILLIPS⁹

Draft version October 25, 2018

ABSTRACT

We present extensive multiwavelength (radio to X-ray) observations of the Type Ib/c SN 2013ge from -13 to $+457$ days relative to maximum light, including a series of optical spectra and *Swift* UV-optical photometry beginning 2 – 4 days post explosion. This makes SN 2013ge one of the best observed normal Type Ib/c SN at early times, when the light curve is particularly sensitive to the progenitor configuration and mixing of radioactive elements. These early observations reveal two distinct light curve components in the UV bands. The first component rises over 4 – 5 days and is visible for the first week post-explosion. Spectra of the first component have a blue continuum and show a plethora of high velocity ($\sim 14,000$ km s⁻¹) but narrow (~ 3500 km s⁻¹) spectroscopic features, indicating that the line forming region is restricted. The explosion parameters estimated for the bulk explosion ($M_{\text{ej}} \sim 2 - 3 M_{\odot}$; $E_{\text{K}} \sim 1 - 2 \times 10^{51}$ ergs) are standard for Type Ib/c SN, while detailed analysis of optical and NIR spectra identify *weak* He features at early times (in an object which would have otherwise been classified as Type Ic), and nebular spectra show evidence for mixing and asymmetry in the bulk ejecta. In addition, SN 2013ge exploded in a low metallicity environment ($\sim 0.5 Z_{\odot}$) and we have obtained some of the deepest radio and X-ray limits for a Type Ib/c SN to date that constrain the progenitor mass-loss rate to be $\dot{M} < 4 \times 10^{-6} M_{\odot} \text{ yr}^{-1}$. We are left with two distinct progenitor scenarios for SN 2013ge depending on our interpretation of the early emission. If the first component is cooling envelope emission, then the progenitor of SN 2013ge possessed a low-mass extended ($\gtrsim 30 R_{\odot}$) envelope. Alternatively, if the first component is due to outwardly mixed ⁵⁶Ni then our observations are consistent with the asymmetric ejection of a small amount of mass ($\sim 0.05 M_{\odot}$) ahead of the bulk explosion. Current models for the collision of a SN shock with a binary companion cannot reproduce both the timescale and luminosity of the early emission in SN 2013ge. Finally, we find that the spectra of the first component of SN 2013ge are similar to those of the rapidly-declining SN 2002bj.

Subject headings: supernovae:general; supernova:individual(SN2013ge)

1. INTRODUCTION

mdrout@cfa.harvard.edu

¹ Harvard-Smithsonian Center for Astrophysics, 60 Garden Street, Cambridge, MA 02138

² Astrophysical Institute, Department of Physics and Astronomy, 251B Clippinger Lab, Ohio University, Athens, OH 45701, USA

³ Steward Observatory, University of Arizona, 933 North Cherry Avenue, Tucson, AZ 85721, USA

⁴ Einstein Fellow

⁵ Department of Astronomy, The Ohio State University, 140 West 18th Avenue, Columbus, OH 43210, USA

⁶ NASA Goddard Space Flight Center, Greenbelt, MD 20771, USA

⁷ Department of Astronomy, University of California, Berkeley, CA 94720-3411, USA

⁸ Department of Physics and Astronomy, Aarhus University, Ny Munkegade 120, 8000 Aarhus C, Denmark

⁹ Carnegie Observatories, Las Campanas Observatory, Colina El Pino, Casilla 601, Chile

¹⁰ Itagaki Astronomical Observatory, Teppo-cho, Yamagata, Yamagata 990-2492, Japan

¹¹ Observatories of the Carnegie Institution for Science, 813 Santa Barbara Street, Pasadena CA 91101, USA

¹² Boise State University, Dept. Of Physics, 1910 Univ. Drive Boise, Boise ID 83725 USA

¹³ Department of Astronomy, University of Texas at Austin, Austin, TX 78712, USA

Type Ib/c supernovae (SN) are an observational subclass of stellar explosions which are identified mainly by the lack of either strong hydrogen or strong silicon features in their optical spectra (see Wheeler et al. 1995, Filippenko 1997 for a review of SN classifications). This class can be further divided into Type Ib SN, which show conspicuous lines of helium in their spectra, and Type Ic SN, which do not. These events are physically understood to be the core-collapse of massive stars which were stripped of their hydrogen envelopes. Main progenitor channels include isolated Wolf Rayet (WR) stars with massive winds (Begelman & Sarazin 1986; Woosley & Weaver 1995) and lower mass He stars stripped by binary companions (Wheeler & Levreault 1985; Podsiadlowski et al. 1992; Yoon et al. 2010).

The rising phase of a SN light curve is powered by a combination of two main sources: the radioactive decay of ⁵⁶Ni synthesized in the explosion, and cooling envelope emission produced when the ejecta radiates away energy deposited by the SN shock (e.g. Piro & Nakar 2013). In stripped envelope SN, ⁵⁶Ni dominates a majority of the light curve while cooling envelope emission is only present for a few days post-explosion. As a result, very early observations of Type Ib/c SN provide a particularly sensitive probe of both the structure of the

progenitor star prior to explosion (Nakar & Sari 2010; Rabinak & Waxman 2011; Nakar & Piro 2014) and the degree to which radioactive materials are mixed into the outer ejecta (Dessart et al. 2012; Piro & Nakar 2013).

Constraints on the structure of the progenitor star from cooling envelope emission are valuable as the final radii of putative Type Ib/c progenitors are predicted to vary by an order of magnitude or more depending on their initial conditions (mass, metallicity) and evolutionary history (single versus binary) (Yoon et al. 2010). While to date no cooling envelope emission has been observed for a normal (not broad-lined) Type Ic SN, non-detections have been used to place constraints on the progenitor radii in several objects (e.g. PTF10vgv; Corsi et al. 2012) and the shock break out and cooling envelope phase serendipitously observed for the Type Ib SN 2008D constrain its progenitor radius to be $\lesssim 12 R_{\odot}$ (Soderberg et al. 2008).

In addition, a handful of SN with double peaked optical light curves have been discovered in recent years. When interpreted as cooling envelope emission the first peak implies that the progenitor star possessed a low-mass extended envelope which varies from the standard hydrostatic models of stellar structure (Nakar & Piro 2014; Bersten et al. 2012; Nakar 2015). While a majority of these events are of Type IIb (e.g. SN 1993J Wheeler et al. 1993; SN 2011dh Arcavi et al. 2011; SN 2013df Van Dyk et al. 2014) such a phenomena has also been observed in the Type Ibc SN iPTF 13beo (Gorbikov et al. 2014) and the Ic-BL SN 2006aj associated with GRB 060218 (Campana et al. 2006; Nakar 2015). X-ray observations also point to a subset of long GRB progenitors which either underwent mass-loss in the final years before explosion or possess low-mass, extended, progenitor envelopes (Margutti et al. 2015), further emphasizing holes in our understanding of the final state of the progenitors for some SN.

Constraints on the mixing of radioactive material from rising light curves can also provide insight into the progenitor structure and explosion mechanism for various subclasses of Type Ib/c SN. Mixing in core-collapse SN can be accomplished by a number of mechanisms (see Dessart et al. 2012, and references therein) including a large-scale asymmetry of the explosion (e.g. a “jet”-like explosion), a large-scale asymmetry of the SN shock produced by the neutrino or magneto-rotational mechanism (e.g. Scheck et al. 2006; Marek & Janka 2009; Maeda et al. 2002; Burrows et al. 2007), and smaller-scale Rayleigh-Taylor and Kelvin Helmholtz instabilities developing at the shock front (an effect which is expected to be stronger in low-mass, extended, progenitors; Kifonidis et al. 2006; Joggerst et al. 2009; Hammer et al. 2010). The observed signature of such mixing will vary depending on its origin, ranging from small modifications to the timescale and colors on the rise for well-mixed shallow deposits of ^{56}Ni (Dessart et al. 2012) to double peaked light curves for asymmetric ejections of material, as has been invoked for the Type Ib SN 2005bf (Folatelli et al. 2006; Tanaka et al. 2009).

Understanding the mixing of radioactive material is especially vital for constraining what distinguishes whether a given progenitor will explode as a Type Ib or Ic SN. The production of He I lines in SN spectra requires non-thermal excitation of the He atoms, likely from the γ -

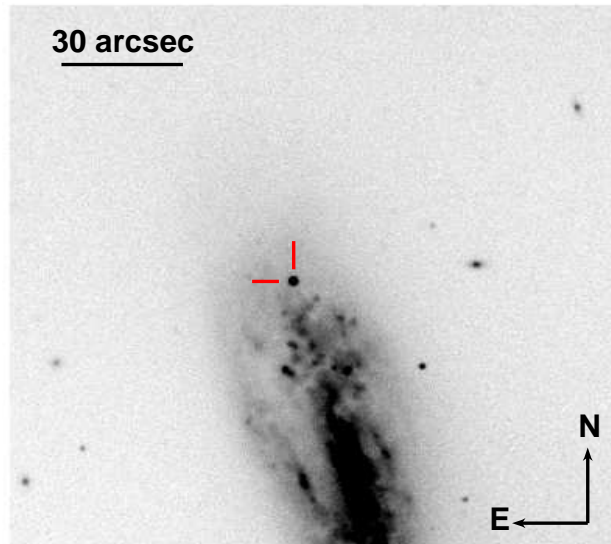


FIG. 1.— r-band image from MMTCam obtained on 2014-04-01 showing the location of SN 2013ge (red cross hairs) on the outskirts of NGC 3287.

rays produced by the radioactive decay of ^{56}Ni (e.g. Lucy 1991; Dessart et al. 2012; Hachinger et al. 2012). Thus, in order to produce a Type Ib SN, mixing may be required, while the observation of a Type Ic SN does not necessarily imply that its progenitor was He poor. Early observations which constrain mixing in a normal Type Ic SN can therefore help to distinguish whether or not these events have an intrinsically lower He abundance.

Thus, particularly when they are coupled with other multiwavelength observations, early light curves offer us insight into topics such as the evolutionary path of the progenitor, the explosion mechanism, and the properties which dictate whether a given star will explode as a Type Ib or Ic SN. In this paper we present detailed observations of the Type Ib/c SN 2013ge, which span radio to X-ray and include spectroscopic and UV-optical photometry beginning 2–4 days after our inferred epoch of first light. These early observations show behavior which has not been observed in any Type Ib/c SN to date: a distinct light curve component is visible in the blue bands for the first week after explosion and the spectra on the rising portion of this early component show high velocity, but *narrow* P Cygni features.

In Section 2 we describe the observations obtained for SN 2013ge. In Sections 3, 4, we describe the photometric and spectroscopic properties of SN 2013ge, respectively, while in Section 5 we examine the properties of the circumstellar medium (CSM) surrounding the progenitor star. In Section 6 we discuss the consequences of various observed properties on our understanding of the progenitor of SN 2013ge, and Type Ib/c SN in general.

2. OBSERVATIONS

2.1. Discovery Photometry and Pre-Explosion Limit

SN 2013ge was discovered by Koichi Itagaki on 8.8 Nov. 2013 (all times UT) at a unfiltered magnitude of 16.8 mag using the 0.5-m reflector at the Takanezawa station, Tochigi-ken (CBAT 3601). The location of the transient

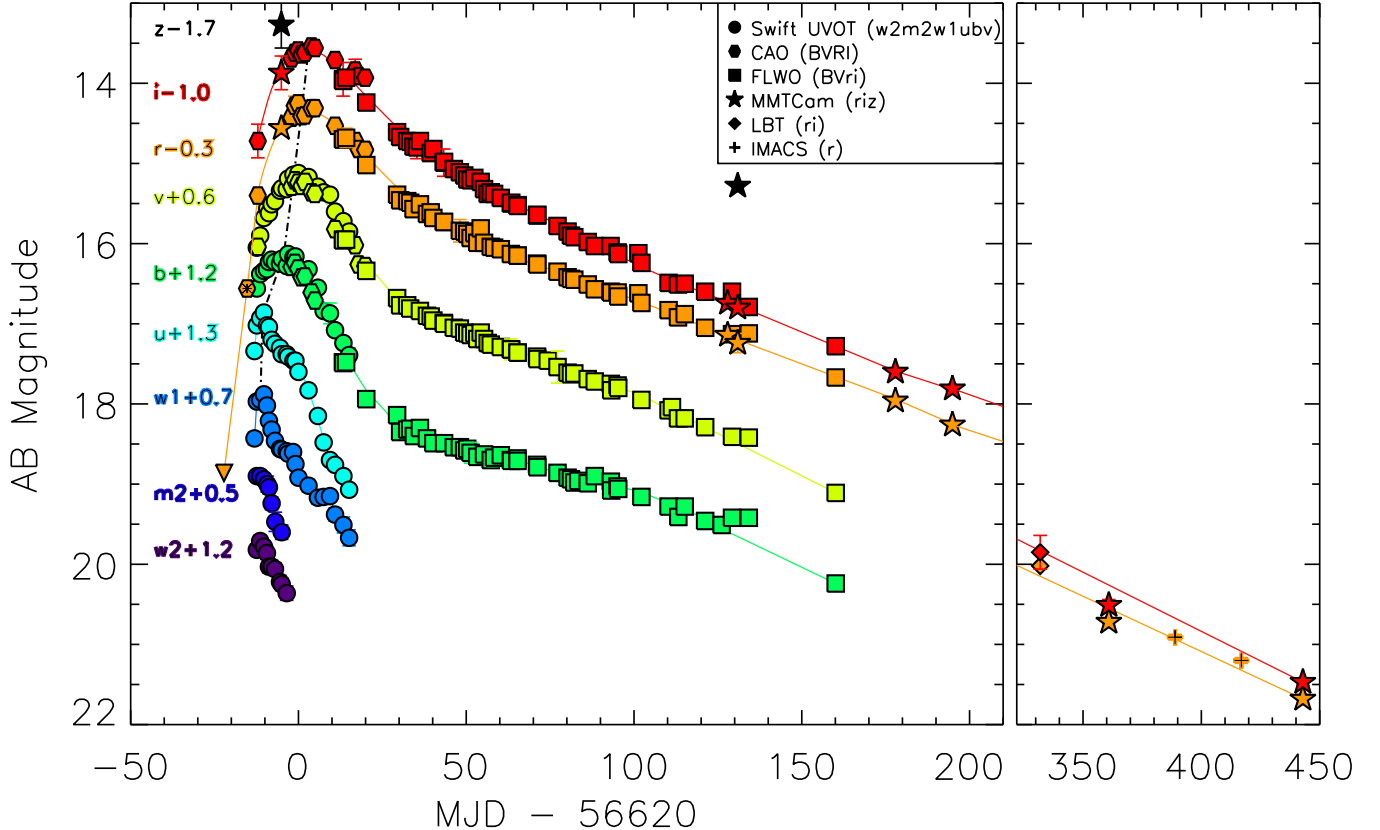


FIG. 2.— Multi-band photometry for SN2013ge spanning -13 to $+457$ days from V-band maximum. Symbol shape indicates the source of the photometry and color the observed band, as labeled. The discovery photometry and pre-explosion limit are shown as an orange hexagon with an asterisk and a downward facing triangle, respectively.

on the outskirts of NGC 3287 is shown in Figure 1. Prior to discovery, SN2013ge was undetected by K. Itagaki on 1.7 Nov. 2013 to an unfiltered magnitude of 18.5 mag. The discovery photometry and pre-explosion limit, re-analyzed for this work, are shown in Figure 2.

2.2. Swift UVOT Photometry

We observed SN2013ge with the UV Optical Telescope onboard *Swift* (UVOT, Gehrels et al. 2004, Roming et al. 2005) from 2013 Nov. 11 to 2013 Dec. 9. The *Swift*-UVOT photometric data have been extracted following the prescriptions of Brown et al. (2009). We used a variable aperture with radius $3'' - 5''$ to maximize the signal-to-noise ratio as the SN flux faded. The *Swift*-UVOT photometry reported in Table 1 and shown in Figure 2 is based on the photometric system described in Breeveld et al. (2011).

2.3. Challis Observatory Optical Photometry

We observed SN2013ge with the Challis Astronomical Observatory (CAO) on 12 nights spanning 2013 Nov. 12 to 2013 Dec 14 (-10 days to $+22$ days). CAO is located in central Idaho near the River of No Return Wilderness. The facility telescope is a 0.4-m $f/10$ Meade LX-200, equipped with an Apogee Alta U47-MB camera (1024^2 pixels) and UBVRi Bessell filters.

For each epoch, $5 - 10$ individual images were stacked and PSF photometry was performed using the standard

packages in IRAF¹⁴. Absolute calibration was performed using SDSS observations of field stars. Observations of the field stars were converted from SDSS filters to the BVRI system using the equations of Smith et al. (2002). These data are shown as hexagons in Figure 2 and listed in Table 2.

2.4. FLWO 1.2-m Optical Photometry

We obtained 55 epochs of BVri photometry of SN2013ge spanning 2013 Dec. 7 to 2014 May 3 ($+15$ to $+162$ days) with the Fred Lawrence Whipple Observatory (FLWO) 1.2 meter telescope plus KeplerCam CCD. The KeplerCam data are reduced using IRAF, IDL and PERL procedures as described in Hicken et al. (2012). No host galaxy subtraction was performed. The BVri instrumental magnitudes were measured with point spread function (PSF) fitting using the methods described in Hicken et al. (2012). Photometric zero points were determined by measuring the magnitudes of local comparison stars in the SN2013ge field and Landolt standard stars fields (Landolt 1992) at a variety of airmasses on 5 clear photometric nights. The linear transformation equations were calibrated using Landolt (1992) standards for BV and Smith et al. (2002) standards for r and i bands for each of the 5 photometric clear nights. These data are

¹⁴ IRAF is distributed by NOAO, which is operated by the Association for Research in Astronomy, Inc. under cooperative agreement with the NSF.

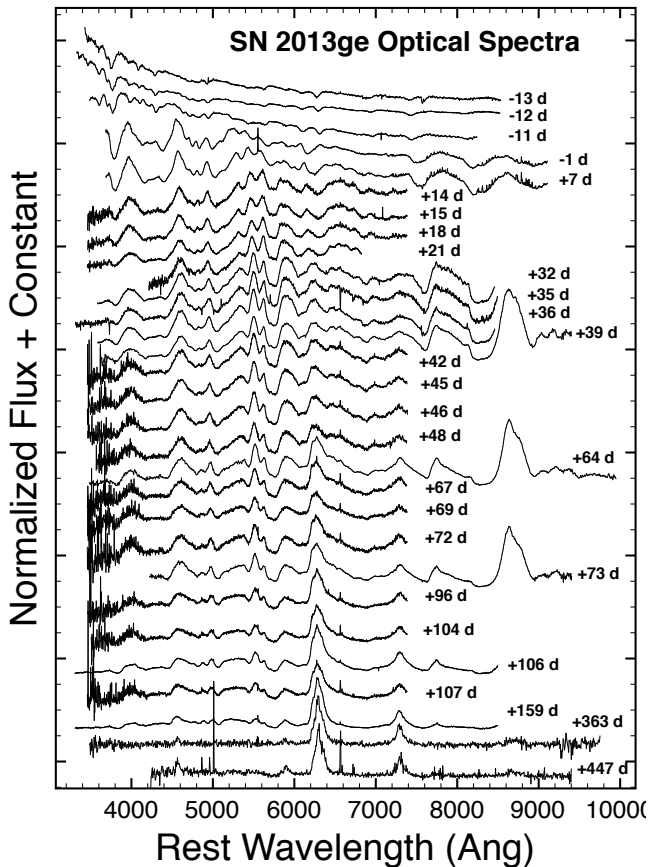


FIG. 3.— Normalized optical spectra spanning -13 d to $+447$ days with respect to V-band maximum.

shown squares in Figure 2 and listed in Table 3.

2.5. MMTCam, LBT and IMACS Optical Photometry

In addition, we obtained eight epochs of ri-band photometry and two epochs of z-band photometry of SN 2013ge with the MMTCam instrument mounted on the 6.5m MMT telescope, one epoch of ri-band imaging with the Large Binocular Camera (LBC; Speziali et al. 2008) mounted on the Large Binocular Telescope (LBT), and two epochs of r-band imaging with IMACS on Magellan-Baade. One epoch was obtained on 2013 Nov. 19 (-3 days), and the other epochs span 2013 Apr. 1 to 2015 Apr. 16 ($+129$ to $+510$ days). For each epoch, bias and flat field corrections were made and individual exposures were stacked using standard routines in IRAF. Dark frame correction were also made for images taken with MMTCam. PSF photometry was performed and absolute calibration was carried out using SDSS observations of field stars. These data are shown in Figure 2 and listed in Table 4.

2.6. X-ray: Chandra

We obtained deep X-ray limits of SN 2013ge with the *Chandra* X-ray Observatory on 2013 Dec. 7 under an approved Director Discretionary Time Proposal (PI Margutti). The total exposure time was 18.8 ks. *Chandra* ACIS-S data were reduced with the CIAO software package (v4.5) and relative calibration files, applying standard filtering criteria. Using *wavedetect* we find no

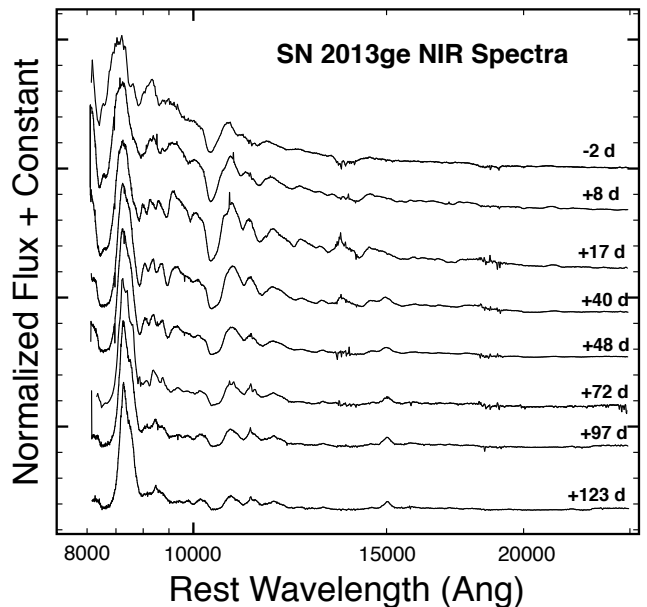


FIG. 4.— Normalized NIR spectra spanning -2 d to $+123$ days with respect to V-band maximum.

evidence for X-ray emission at the location of SN 2013ge. The 3σ count-rate upper limit is $3.1 \times 10^{-4} \text{ cs}^{-1}$ (0.5–8 keV energy band).

The neutral hydrogen column density in the direction of the SN is $N_{\text{Hgal}} = 1.9 \times 10^{20} \text{ cm}^{-2}$ (Kalberla et al. 2005). From our optical spectra we estimate $E(B-V)_{\text{host}} = 0.047$ mag (Section 2.10). For a Galactic dust to gas ratio, this value corresponds to an intrinsic neutral hydrogen column density of $N_{\text{Hhost}} \sim 3 \times 10^{20} \text{ cm}^{-2}$. For an assumed simple power-law spectral model with spectral photon index $\Gamma = 2$ we find an unabsorbed flux limit $3.4 \times 10^{-15} \text{ erg s}^{-1} \text{ cm}^{-2}$ (0.3–10 keV). At the distance of 23.7 Mpc (Section 2.10), the flux above translates into a luminosity limit of $2.3 \times 10^{38} \text{ erg s}^{-1}$.

2.7. Radio: VLA

We obtained three epochs of deep radio limits for SN 2013ge at 4.8 and 7.1 GHz with the VLA in B configuration¹⁵. Observations were obtained on 2013 Nov. 16, 25, and 2014 Jan. 14 (-6 , $+3$, and $+53$ days).

All observations were taken in standard continuum observing mode with a bandwidth of 16×64 MHz. During the reduction we split the data in two side bands (8×64 MHz) of approximately 1 GHz each. We used 3C286 for flux calibration, and for phase referencing we used calibrator J1018+3542. Data were reduced using standard packages within the Astronomical Image Processing System (AIPS). No radio emission was detected from SN 2013ge in any of these observations and the upper limits are listed in Table 5.

2.8. Optical Spectroscopy

29 epochs of low resolution optical spectra were obtained for SN 2013ge, spanning -13 days to $+447$ days.

¹⁵ The National Radio Astronomy Observatory is a facility of the National Science Foundation operated under cooperative agreement by Associated Universities, Inc.

In addition, one moderate resolution ($R \sim 3400$) spectrum was obtained at -12 days in the region of NaID. All optical spectra are listed in Table 6 and shown in Figure 3.

Initial reduction (overscan correction, flat fielding, extraction, wavelength calibration) of all standard long slit spectra was carried out using the standard packages in IRAF. The MODS/LBT spectrum was taken in the dual channel mode with gratings G400L and G670L, and we used the modsCCDRed suite of python programs to perform bias subtraction, flat-field correction, and adjust for bad columns, before extracting the spectrum using standard packages in IRAF. Flux calibration and telluric correction for all long slit spectra were performed using a set of custom idl scripts (see, e.g., Matheson et al. 2008; Blondin et al. 2012) and standard star observations obtained the same night as the science exposures. Spectra obtained with the Hectospec multi-fiber spectrograph (Fabricant et al. 2005) were reduced using the IRAF package “hectospec” and the CfA pipeline designed for this instrument.

2.9. Infrared Spectroscopy

We obtained 8 epochs of NIR spectra of SN 2013ge with the Folded-port InfraRed Echellette spectrograph (FIRE; Simcoe et al. 2013) on Magellan-Baade spanning -2 to $+123$ days. These data were reduced following standard procedures (Hsiao et al. 2013) using a custom-developed IDL pipeline (FIRE-HOSE). All NIR spectra are listed in Table 6 and shown in Figure 4.

2.10. Distance and Reddening

SN 2013ge exploded on the outskirts of NGC 3287. In this paper we adopt of distance of 23.7 ± 1.7 Mpc, corresponding to the NED distance after correction for Virgo, Great Attractor, and Shapley Supercluster infall, assuming $H_0 = 73 \text{ km s}^{-1} \text{ Mpc}^{-1}$ (Mould et al. 2000).

Milky Way reddening in the direction of SN 2013ge is $E(B-V)_{\text{MW}} = 0.020$ mag (Schlafly & Finkbeiner 2011). In order to estimate any intrinsic absorption due to dust within NGC 3287, we examine our moderate resolution spectra obtained on 2014-11-10 for narrow NaID absorption lines. We identify two NaID $\lambda\lambda 5889.9, 5895.9$ doublets, one corresponding to Milky Way absorption, and one at the redshift of NGC 3287. The total equivalent width of the NaID doublet at the redshift of NGC 3287 is $\sim 0.45 \text{ \AA}$. Using the empirical relation of Poznanski et al. (2012) this implies a host galaxy contribution to the total reddening of SN 2013ge of $E(B-V)_{\text{host}} = 0.047$ mag. Thus, throughout this paper we adopt an $R = A_V/E(B-V) = 3.1$ Milky Way extinction curve with a total reddening of $E(B-V)_{\text{tot}} = 0.067$ mag. This value is consistent with that derived from the $V-R$ color method described in Drout et al. (2011).

3. PHOTOMETRIC PROPERTIES

3.1. Light Curve Evolution

A deep pre-explosion limit for SN 2013ge was obtained 7 days prior to its initial discovery. However, the rapid rise observed in the initial *Swift* u- and w1- bands (which began ~ 2 days after first detection; see Figure 5) indicate that our constraints on the epoch of first light are more stringent than allowed by this non-detection alone. Extrapolating polynomial fits of the rising phase

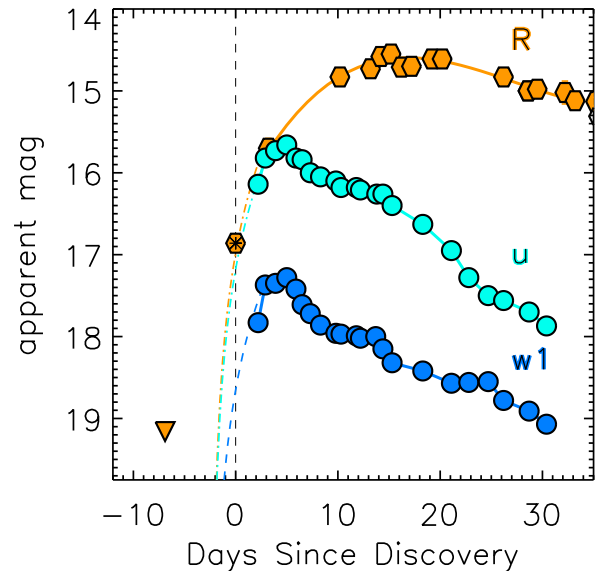


FIG. 5.— Characterization of the epoch of first light. Shown are the R-band (orange), u-band (cyan), and w1-band (blue) light curves. The rapid rise observed during the first epochs of the u- and w1- put tight constraint on the epoch of first light of this light curve component. Dashed colored lines are power law fits of the form $t^{1.5}$ to the rising portion of each curve, each of which imply an epoch of first light 2 days prior to first detection.

of these light curves backward in time, we infer an epoch of only ~ 2 day prior to first detection. Power-law fits of the form $L_\lambda \propto t^{1.5}$ and $L_\lambda \propto t^2$ yield similar results. The former power law is expected for the rising phase of cooling envelope emission (e.g. Piro & Nakar 2013) and the latter is expected for early radioactive heating in the fireball model (Nugent et al. 2011). Throughout this paper we adopt an epoch of first light of 2014 Nov. 6.5 = MJD 56602.5 ± 2 days. An epoch of first light prior to this date would be inconsistent with the early u- and w1- band light curves unless the rate of rise *increased* some time post-explosion. Such behavior is not typically observed in SN light curves, and would have implications for the emission source which will be discussed in Section 6, below. The possibility of a “dark period” separating the epoch of first light from the explosion epoch (Piro & Nakar 2013) will be also discussed in Section 6.

In Table 7 we list basic properties derived for the UV and optical light curves of SN 2013ge based on low order polynomial fits. Throughout this paper, phase of the SN will be given with respect to V-band maximum light: MJD 56618.6. This time of maximum implies a rise time in the V-band of ~ 16 days. As is observed in other Type I SN, the time of maximum light cascades through the UV and optical bands (as shown by the dashed dotted line in Figure 2). SN 2013ge peaks at an absolute magnitude of approximately -17.3 mag (AB) in the optical, and decays between 1.1 mag and 0.38 mag in the first 15 days post maximum light ($B-$ though $I-$ bands, respectively). This places SN 2013ge at both the low luminosity and slowly-evolving end of Type I SN.

The BVRI light curves are characterized by a smooth rise to maximum light, followed by an initial decline and

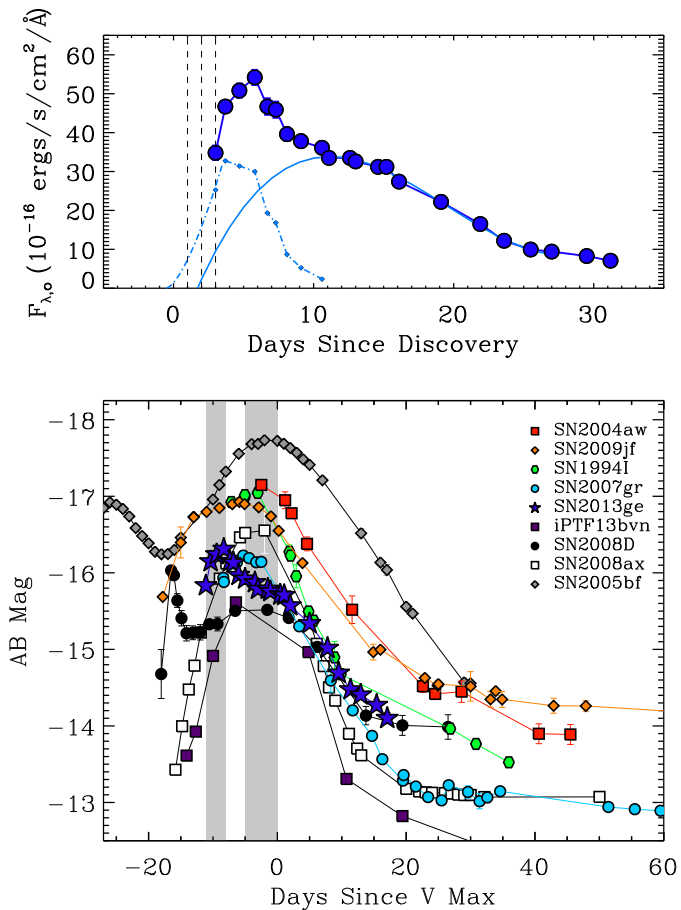


FIG. 6.— *Top*: Example decomposition of the u-band light curve into two components. This should be taken as representative only as we do not constrain the rising behavior of the second component. Dashed vertical lines represent our first three epochs of spectroscopy, which occur on the early rising portion of the first light curve component. *Bottom*: Comparison of the u-band light curve of SN 2013ge to other stripped core-collapse SN. Grey shaded bands highlight the peak time for the two components of SN 2013ge. A majority of events peak on a timescale similar to the second component observed in SN 2013ge. The light curve of SN 2009jf shows a plateau that may be indicative of an early component similar to that observed in SN 2013ge. *References*: SN 2005bf (Folatelli et al. 2006), SN 2004aw (Taubenberger et al. 2006), SN 2009jf (Richmond et al. 1996), SN 2007gr (Hunter et al. 2009), SN 2008ax (Pastorello et al. 2008), SN 2008D (Soderberg et al. 2008), iPTF13bvn (Fremling et al. 2014; Cao et al. 2013).

then a shallowing of the decay slope between 20 and 30 days post maximum light. Linear fits to the BVRI light curves between 60 and 120 days post maximum reveal linear decline rates between 0.01 and 0.02 mag day⁻¹. This light curve morphology is typical for Type I SN.

3.2. Early UV Light Curves

In contrast, the u- and w1- light curves observed for SN 2013ge show a distinctly non-standard evolution. They display an early “bump” which is characterized by a rapid rise and decline over the first week of observations, before plateauing and then falling off rapidly again. In the top panel of Figure 6 we demonstrate that the u-band light curve can be decomposed into two components. A main component which peaks ~ 11 days after discovery superimposed with an early peak of emission which rises

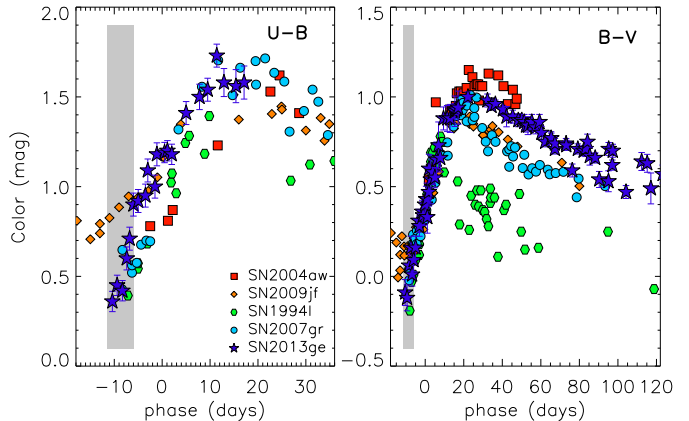


FIG. 7.— U–B (left) and B–V color evolution of SN 2013ge in comparison to other Type Ib/c SN. Shaded grey regions indicate the timeframe of the first light curve component. During the falling portion of the first light curve component (–8 to –5 days) the U–B color reddens drastically. The B–V evolution of SN 2013ge is very similar to other Type Ib/c SN.

rapidly over ~ 4 days and declines rapidly after ~ 1 week. This particular decomposition is for illustrative purposes only, as we do not constrain the rising behavior of the second component. Three vertical dashed lines mark the time of our first three epochs of spectroscopy, which probe the early rising portion of the first component.

Although well sampled u-band light curves between –14 and –7 days relative to maximum light are still quite rare for Type I SN, no previous object has shown two distinct components with these timescales. This is demonstrated in the lower panel of Figure 6 where we compile u-band light curves from the literature. A majority of events peak ~ 4 days prior to V-band maximum and then decline rapidly, consistent with our inferred time of maximum and subsequent evolution for the *second* component in SN 2013ge.

Prior to this maximum, the evolution of the literature events are varied. Both SN 2008D and SN 2005bf also show double peaked u-band light curves, but show significant timescale variations in comparison to the first component in SN 2013ge. The first peak in the light curve of SN 2008D is attributed to shock breakout cooling envelope emission, and rises on a timescale of $\lesssim 1$ day. In contrast, the first peak in the light curve of peculiar Type Ib SN 2005bf has a rise time significantly larger. Intriguingly, the u-band light curve of the Type Ib SN 2009jf shows a plateau which could be consistent with two components similar to those in SN 2013ge if the relative luminosity of the second component were higher, while the Type Ib iPTF 13bvn shows no signs of two components.

3.3. Color Evolution and SEDs

In Figure 7 we plot the $U - B$ and $B - V$ colors of SN 2013ge and several other Type Ib/c SN. The grey shaded region highlights the time of the u-band excess described above. During this time period the u-b color is relatively flat for 3 days and then rapidly reddens from ~ 0.4 mag to ~ 0.9 mag over 4 days, before continuing to redden at a slower rate. The $B - V$ evolution of

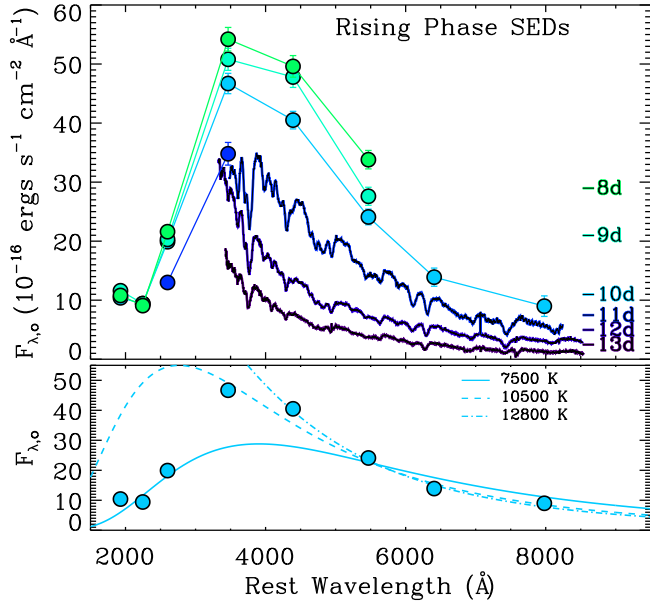


FIG. 8.— Rising phase SEDs of SN 2013ge. *Top*: Spectra and broadband photometry obtained on the rising phase of the first light curve component. Our earliest spectra, obtained before broadband photometry, show a steep blue continuum with narrow superimposed spectral features. Our first epoch of UVOT photometry (-11 days) constrains the peak of the SED to be around 3500 Å. *Bottom*: The -10 day SED with superimposed blackbody fits. It is not possible to fit both the slope of the SED in the optical and the depressed UV flux with a single temperature blackbody, indicating that line blanketing may be important even at these early epochs.

SN 2013ge is similar to other Type Ib/c SN.

In Figure 8 we plot the spectral energy distribution of SN 2013ge for epochs on the rising phase of the initial u-band peak (including our first three epochs of spectroscopy). The first spectroscopic observations are characterized by a very blue continuum and from day -11 onward we constrain that the SED falls off significantly in the UV-bands. However, as shown in the lower panel of Figure 8 where we fit blackbodies to various sub-sets of the -10 day SED, it is not possible to fit both the slope of the optical SED and the low flux level in the UV-bands with a single blackbody. Such behavior may indicate that even at these very early epochs, line blanketing is significantly depressing the UV-flux.

Fitting blackbodies to the BVRI-bands only we find color temperatures which fall from around $13,000$ K at -12 days to around 7000 K at V-band maximum. The precise temperature evolution during the initial u-band rise is difficult to assess due to (1) the depressed UV flux and (2) our lack of dense R and I-band photometry at the earliest epochs.

3.4. Pseudo-Bolometric Light Curve

To create a pseudo-bolometric light curve for SN 2013ge, we first sum our UV-optical photometry by means of a trapezoidal interpolation. To account for missing IR flux, we then attach a blackbody tail from the best-fit blackbody to the BVRI-data. This method of accounting for IR flux is equivalent to adding an IR of contribution which monotonically increases from 15%

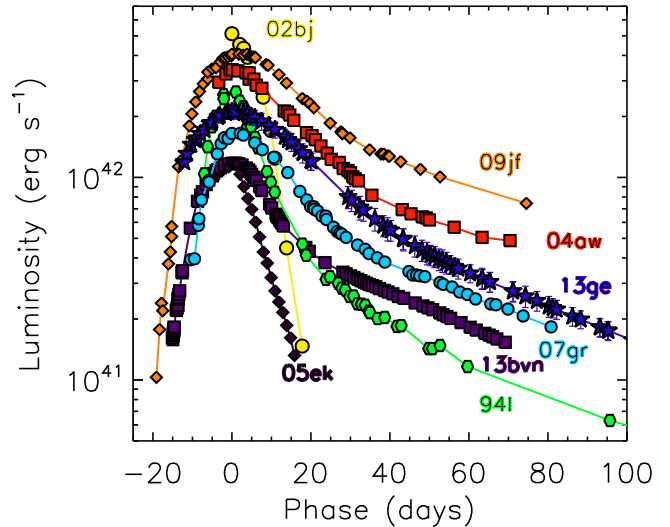


FIG. 9.— Pseudo-bolometric Light Curve of SN 2013ge in comparison to other Type Ib/c SN. SN 2013ge is relatively faint and slowly evolving. Although there are not two distinct peaks in the pseudo-bolometric light curve, the early component visible in the u-band and UV light curves does result in a “shoulder” of excess emission at early times. References for comparison objects: SN 2005ek (Drout et al. 2013), SN 2002bj (Poznanski et al. 2010), SN 2004aw (Taubenberger et al. 2006), SN 2009jf (Valenti et al. 2011), SN 2007gr (Hunter et al. 2009), SN 1994I (Richmond et al. 1996), iPTF 13bvn (Fremming et al. 2014).

at early times to $\sim 50\%$ at late times. This is in line with what is observed in Type I SN with well-observed IR light curves (see, e.g., Valenti et al. 2008). The resulting bolometric light curve is shown in Figure 9 along with the bolometric light curves from other Type I SN. Although two distinct peaks are not evident, an excess shoulder of emission can be seen at early times corresponding to the the first u-band component described above. The bolometric light curve peaks at $2.1 \pm 0.1 \times 10^{42}$ erg s $^{-1}$ and the total radiated energy between -12 and $+120$ days is $8.1 \pm 0.3 \times 10^{48}$ ergs.

Assuming SN 2013ge is powered mainly by the radioactive decay of ^{56}Ni , we use the analytic models of Arnett (1982) and Valenti et al. (2008) with the corrections of Wheeler et al. (2015) to extract estimates of the explosion parameters from this pseudo-bolometric light curve. We assume that from -8 days to $+20$ days SN 2013ge is in the optically thick photospheric phase (we neglect the earliest data, during the “UV bump” when performing our fit), and utilize a constant opacity of 0.07 cm 2 g $^{-1}$ (corresponding to the case of electron scattering). Under these assumptions we find best-fit explosion parameters of $M_{\text{Ni}} \approx 0.12 M_{\odot}$, $M_{\text{ej}} = 2 - 3 M_{\odot}$, and $E_{\text{K}} = 1 - 2 \times 10^{51}$ ergs. We have assumed a photospheric velocity at maximum of $9000 - 10,000$ km s $^{-1}$ in order to break the degeneracy between M_{ej} and E_{K} (see Section 4).

Inserting these best-fit parameters from the photospheric phase in the nebular model from Valenti et al. (2008) we find a predicted luminosity which is relatively consistent with our late-time (> 60 days post-maximum) pseudo-bolometric light curve, although the predicted model declines slightly more rapidly than the observed

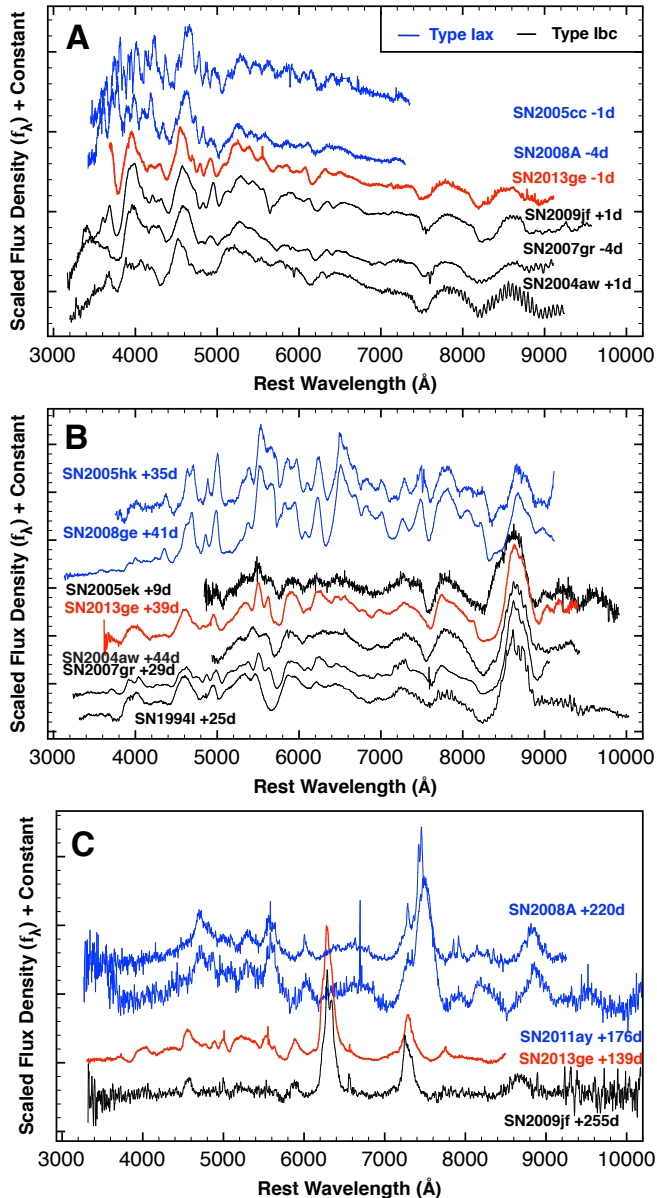


FIG. 10.— Comparison of the spectrum SN 2013ge at maximum light (panel A), intermediate phases (panel B) and late-time (panel C) to spectra of Type Ib/c SN (black) and Type Iax SN (blue). Although there is significant overlap between both classes of objects at maximum light, at intermediate and late phases the evolution of SN 2013ge is similar to Type Ib/c SN. *References:* SN 2005cc and SN 2008A (Blondin et al. 2012), SN 2005hk (Phillips et al. 2007), SN 2008ge (Silverman et al. 2012), SN 2011ay (Foley et al. 2013), SN 2009jf (Valenti et al. 2011), SN 2007gr (Valenti et al. 2008), SN 2004aw (Taubenberger et al. 2006), SN 2005ek (Drout et al. 2013), SN 1994I (Filippenko et al. 1995)

light curve. Such a trend has been noted in the literature when attempting to model Type Ib/c SN with single zone models (see, e.g., Maeda et al. 2003 and Valenti et al. 2008), and may indicate that SN 2013ge could be slightly better described by a two-zone model with a high-density inner region and a low-density outer region. Alternatively, this could be evidence for an asymmetry in the explosion.

4. SPECTROSCOPIC PROPERTIES

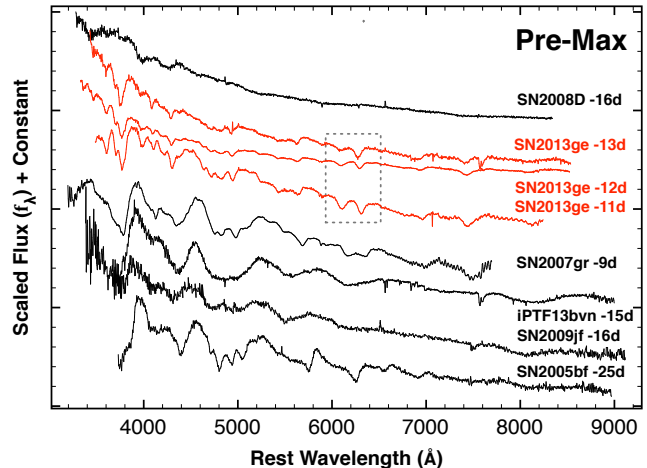


FIG. 11.— Very early spectra of SN 2013ge compared to other Type Ib/c SN. The spectra of SN 2013ge are characterized by a blue continuum and *narrow* spectroscopic features. In contrast, most other Type Ib/c SN at a similar epoch show very broad features. One exception is the Type Ib SN 2005bf which during its first light curve peak showed both broad underlying features and narrow high velocity features of Fe and Ca. In contrast, *all* of the features observed in the early spectra of SN 2013ge have similar high velocities and narrow widths. They dashed grey box highlights two features whose ratio shows significant evolution over ~ 2 days. *References:* SN 2008D (Modjaz et al. 2009a), SN 2007gr (Valenti et al. 2008), iPTF13bvn (Milisavljevic et al. 2013), SN 2009jf (Sahu et al. 2011), SN 2005bf (Folatelli et al. 2006)

4.1. Type Ib/c versus Type Iax

SN 2013ge can be immediately identified as a Type I SN since it lacks *conspicuous* hydrogen emission, and can further be sub-classified as a Type Ib/c from the lack of a strong Si II $\lambda 6355$ feature (Wheeler et al. 1995). Near maximum light, the spectral features are relatively narrow and resemble maximum light spectra of both normal (not broad-lined) Type Ib/c SN and Type Iax SN (Foley et al. 2013). In order to resolve this degeneracy, in Figure 10 we compare spectra of SN 2013ge (red) to spectra of several normal Type Ib/c SN (black) and Type Iax SN (blue) at three phases: maximum light (panel A), transitional¹⁶ (panel B) and nebular (panel C).

Taken in conjunction, it is clear that from maximum light onwards SN 2013ge follows a spectral evolution typical for normal Type Ib/c SN. Near maximum light, iron peak elements are visible at bluer wavelengths as well as OI and the Ca II NIR triplet in the red. By +39 days, SN 2013ge has entered a transitional phase, marked by the onset of increased emission in the CaII NIR triplet. This growth of the Ca II NIR feature has been observed in numerous Type Ib/c SN. Finally, at nebular phases SN 2013ge is dominated by intermediate mass elements such as [O I], [Ca II], and Mg II].

This is in stark contrast to the well observed Type Iax SN, which do not show growth of the CaII NIR triplet at intermediate phases and whose late-time spectra are dominated by forbidden Ca II and Fe II lines with no obvious contribution from [O I]. However, it is worth emphasizing the strong similarity between Type Iax spectra and normal Type Ic spectra at maximum

¹⁶ “transitional” refers to the transition from photospheric phases to nebular phases

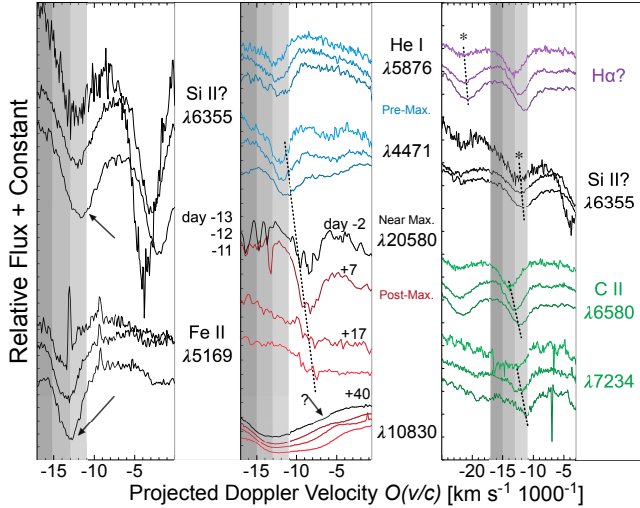


FIG. 12.— Projected doppler velocities around key features in the spectra of SN 2013ge used to assess the presence of various unburned material (hydrogen, helium, and carbon). Grey regions are placed to guide the eye for a constant velocity while dashed lines highlight the velocity evolution of a certain features with time. *Left*: The regions around Si II $\lambda 6355$ and Fe II $\lambda 5169$ in the -13 , -12 , and -11 day spectra. *Middle*: Assessing the presence of Helium both in the early optical spectra and maximum light NIR spectra. See text for details. *Right*: Assessing the degeneracy between $H\alpha$, Si II $\lambda 6355$, and CII $\lambda 6580$. See text for details.

light - especially in the wavelength range $4200 - 7500 \text{ \AA}$. The main differentiating spectral features seem to be at wavelengths shorter than 4200 \AA , where SN Iax show a plethora of lines which are not evident in normal Type Ib/c SN. Caution should be taken in classifying a Type Iax SN from a single maximum light spectrum.

4.2. Early Spectra

Despite evolving similar to normal Type Ic SN from maximum onward, the early spectra of SN 2013ge are unprecedented. Our earliest three spectra, obtained between -13 and -11 days, are characterized by a strong blue continuum, superimposed with relatively shallow and *narrow* features ($\text{FWHM} \lesssim 3500 \text{ km/s}$). These spectra were obtained during the early rising phase of the first u-band component described in Section 3. Spectroscopic observations of Type Ib/c SN at such an early phase are very rare, but a majority of events show *broad* high velocity features at early times, which narrow as the photospheric velocity decreases. Indeed, these spectra vary significantly from the earliest spectra obtained for SN 2008D, SN 2009jf, and iPTF13bvn, all of which showed very broad spectral features at similar epochs (see Figure 11).

During its first light curve peak, the spectra of the peculiar Type Ib SN 2005bf do show several narrow spectroscopic features between 4500 \AA and 5300 \AA (see Figure 11). However, features in the rest of the spectrum are broad and more comparable to the other Type Ib/c SN shown in Figure 11. Folatelli et al. (2006) interpret this as the combination of an underlying spherical photosphere (broad) and high velocity iron and calcium features (narrow). In contrast, in the early spectra of SN 2013ge, *all* of the features observed have similarly narrow widths.

In addition, we observe rapid evolution in both the

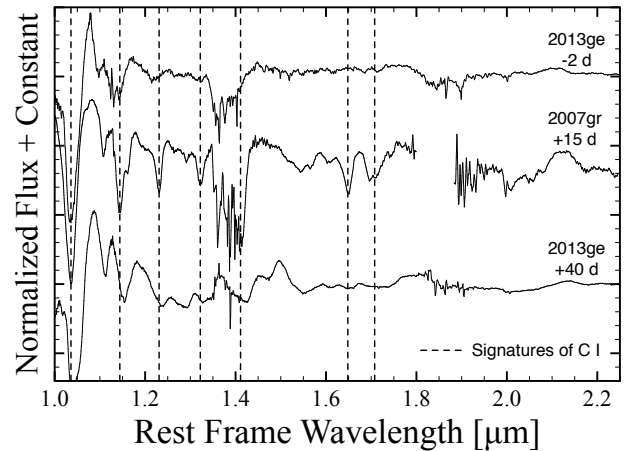


FIG. 13.— Comparisons between IR spectra of SN 2007gr and SN 2013ge. Vertical dashed lines denote C I lines marked by Hunter et al. 2009 in their Fig. 12. Lines of a comparable strength are not observed in SN 2013ge.

slope of the continuum and photospheric velocity over the two day time period in which these spectra were obtained. We draw particular attention to the two absorption features between 6000 and 6500 \AA , which undergo a large change in their ratio over this time period. These features are highlighted by a grey box in Figure 11.

4.3. Assessing the Presence of Unburned Material

For many models, fully stripping the H/He layer from a putative Type Ib/c progenitors has proved challenging, making the possible identification of trace amounts of H and He in the atmospheres of Type Ib/c SN both important and long debated (see Parrent et al. 2014 for a review). Unfortunately, identification of such contaminants is particularly complicated in the optical photospheric spectra of Type Ib/c SN where a number of degeneracies exist, most notably between lines of H I $\lambda 6563$, C II $\lambda 6580$, and Si II $\lambda 6355$, and He I $\lambda 5876$ and Na I $\lambda 5889$. These degeneracies can be partially alleviated if NIR spectra are available.

Our early photospheric phase spectra probe the outermost regions of the ejecta where unburned material such as hydrogen and helium are most likely to be present, if at all. In Figure 12 we attempt to identify various spectral features by cross-examining our earliest three optical spectra (days -13 , -12 , -11) along side later evolution at IR wavelengths. Here we have shifted the spectra from the rest frame to projected Doppler velocities of commonly found lines in order to offer up preliminary matches between spectral features and dominant candidate lines.

4.3.1. Hydrogen

When we associate Si II $\lambda 6355$ and Fe II line signatures in the left panel of Figure 12, it can be seen that expansion velocities are $\sim 14,000 \text{ km s}^{-1}$ (grey vertical bands are placed to guide the eye). This highlights that the lines in these early spectra are *both* high velocity and narrow. However, it can also be seen that the feature most often associated with Si II $\lambda 6355$ appears at slightly lower velocities than Fe II, which would suggest that photons from layers deeper within are somehow

penetrating opaque lines of Fe II. This discrepancy between Si II and Fe II has been seen previously (e.g. SN Ib 1999dn and 2005bf Elmhamdi et al. 2007; Parrent et al. 2007; SN Ic 1994I Branch et al. 2006; and SN Ic–BL 2012ap Milisavljevic et al. 2015), and it was recently examined in detail for a large number of Type I events in Parrent et al. (2015).

This discrepancy likely indicates that another ion is contributing to the observed line. In core-collapse SN, a strong candidate in this wavelength region is high velocity H α (Wheeler et al. 1995; Benetti et al. 2011; Parrent et al. 2015). In the top portion of the right panel of Figure 12 dashed lines indicate the velocities of each ion (Si II versus H I) which would be necessary to overlap with the observed feature. Unfortunately, we lack certain detections of either Si II λ 5872 or H β in the early spectra of SN 2013ge, and therefore we cannot definitively confirm their relative contributions to the observed feature.

4.3.2. Helium

In the middle panel of Figure 12, we examine the case for He I in the spectra of SN 2013ge. At the top of the panel we show the earliest optical spectra in the region of He I λ 5876, 4471 and find evidence for both lines at similar velocities that also correspond to estimates from the Fe II compound feature.

In the lower portion of the panel, we examine four NIR spectra (-2 to $+38$ days) in the region around the $1\mu\text{m}$ and $2\mu\text{m}$ He I features. The large $1\mu\text{m}$ feature is significantly broader than the $2\mu\text{m}$ feature, and is likely a blend of multiple ions including C I and Si I (Millard et al. 1999; Taubenberger et al. 2006). We identify a feature near $1\mu\text{m}$ which, as highlighted by the dotted line, is consistent with He I at lower photospheric velocity. Thus, we find that there is room for the existence of He I λ 4471, 5876, 10830, and 20580. In addition, the identification of weak optical signatures of He I is consistent with either weak or absent signatures of He I λ 6678 and 7065 (Branch et al. 2002; Parrent et al. 2007; Hachinger et al. 2012)

We therefore conclude that *He I can be robustly identified in the early spectra of SN 2013ge*. However, we emphasize that these lines are weak and fade with time. They are distinct from the strong He I features observed in many SN classified as Type Ib, which are strongest a few weeks past maximum (e.g. Filippenko 1997). *SN 2013ge therefore represents the detection of weak He features in an event which would generally be classified as Type Ic*.

4.3.3. Carbon

Finally, in the lower portion of the right panel of Figure 12 we identify signatures of C II λ 6580, 7234 in the early spectra of SN 2013ge. We also examine our NIR spectra for evidence of C I features at later epochs (Figure 13). While we cannot rule out weak contamination from C I, the influence must be substantially weaker than those observed in the NIR spectra of the “carbon-rich” SN 2007gr (Hunter et al. 2009).

4.4. Species Identification and Estimation of Expansion Velocities

In order to further constrain the full set of ions present in the spectra of SN 2013ge, as well as the evolution of

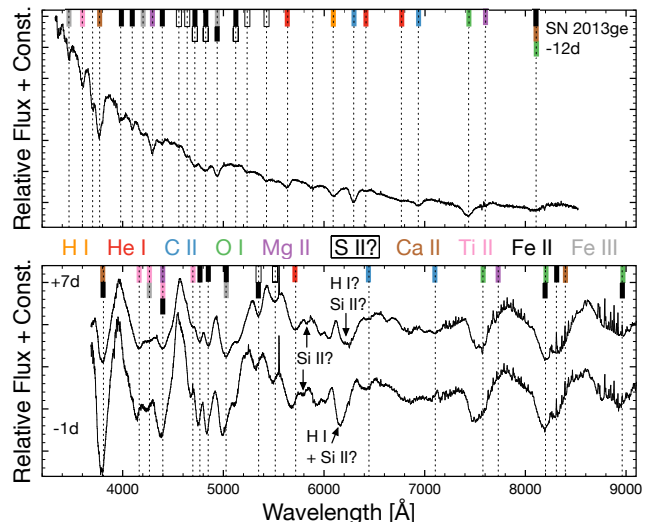


FIG. 14.— Ion identifications in the early (top panel) and maximum light (bottom panel) spectra of SN2013ge. Colored rectangles designate the ions which likely contribute to each feature in the spectra, as labeled between the panels. Species identified include He I, C II, and O I (likely unburned material) as well as contributions from Mg II, Si II, Ca II, Ti II, Fe II, Fe III and possibly Si II. Between -12 days and maximum light the blue continuum is significantly depressed. See text for more details.

the photospheric velocity, we utilize the fast and publicly available spectral synthesis code SYN++ (Thomas et al. 2011).¹⁷ Line formation in SYN++ is assumed to be dominated by pure resonant scattering with Boltzmann statistics determining relative line strengths for a given ion. We use an exponential optical depth profile which begins as the (sharp) photospheric velocity which is set by hand for each epoch. See Parrent (2014) for general fitting methods and procedures.

In Figure 14 we detail line identifications inferred with SYN++. Fits will be refined and provided in a future work. For the photospheric phase spectra of SN 2013ge, we tested a full list of ionization species (H I through Fe II). Each tick mark in the top panel of Figure 14 represents the location of tentatively detectable species, including He I, C II, and O I (likely unburned material) as well as contributions from Mg II, Ca II, Ti II, Fe II, Fe III and possible Si II and S II.

The model photosphere is estimated to decrease from $\sim 14,000 \text{ km s}^{-1}$ to $\sim 12,000 \text{ km s}^{-1}$ between -13 days and -11 days, which is similar to the early velocity evolution seen in SN 2008D (Modjaz et al. 2009b). In order to reproduce both these relatively high velocities and the narrow ($\lesssim 3500 \text{ km s}^{-1}$) width of the features with SYN++ we set the minimum velocity parameter, v_{min} , for all of the ions to $\sim 14,000 \text{ km s}^{-1}$ while that of the model photosphere, v_{phot} , was set to $10,000 \text{ km s}^{-1}$. Within the semi-empirical metric space of SYN++, this is equivalent to the process by which one typically adds “detached” high velocity features to the spectrum. We emphasize that in this case this process was applied to all of the ions present and all to the same velocity and is not meant to suggest a physically detached region from a luminous source; the physical interpretation of these early spectra

¹⁷ This is an updated version of SYNOW; <https://c3.lbl.gov/es/>.

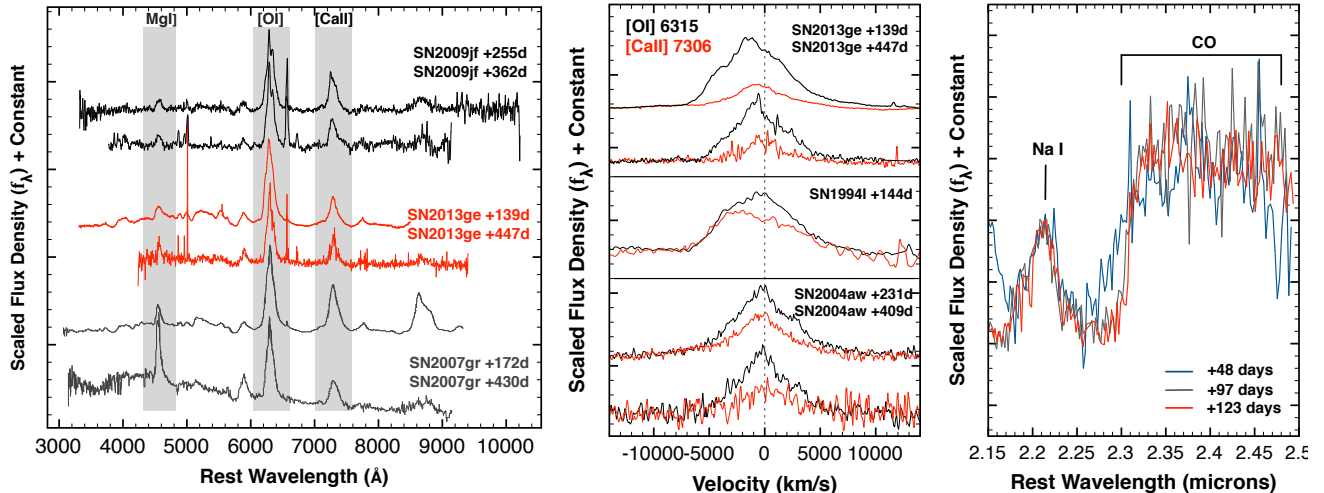


FIG. 15.— *Left*: Comparison of SN 2013ge, SN 2007gr, and SN 2009jf nebular spectra at multiple epochs. At ~ 150 – 250 days, all have a Mg I λ 4571 / [OI] $\lambda\lambda$ 6300, 6364 ratio of ~ 0.15 . However, by ~ 450 days, the ratio in SN 2007gr has grown substantially to ~ 1 , while it has remained relatively constant in SN 2013ge and SN 2009jf. *Center*: Nebular line profiles of SN 2013ge in comparison to SN 1994I and SN 2004aw at a variety of epochs. By late times the [OI] feature in SN 2013ge more closely resembles the peaked structure observed in SN 2004aw, which may be indicative of an asymmetry in the ejecta. *Right*: The CO band head observed in SN 2013ge at three epochs. We observe evolution of the profile between +48 and +97 days. *References*: SN 2009jf (Valenti et al. 2011), SN 2007gr (Chen et al. 2014), SN 2004aw (Taubenberger et al. 2006), SN 1994I (Filippenko et al. 1995)

will be discussed in Section 6, below.

By day -1 , a similar set of ions are inferred as in the day -12 spectrum, although significant evolution is observed. For instance, the spectrum is now significantly redder, a substantive Ti II absorption trough has formed between 4000 Å and 4500 Å, and the strength of the He I and C II features have decreased significantly with respect to the 6250 Å feature (which may have contributions from both Si II and H I, as described above). In addition, the photospheric velocity has decreased to $\sim 10,000$ km s^{-1} (typical for Type Ib/c SN at maximum light) and the width of the features are relatively well matched to the velocity of their absorption minima. Unfortunately, poor weather prohibited us from obtaining any spectra between -11 and -1 days, so we were unable to survey the evolution from narrow high velocity features in the early spectra toward moderate width and velocities in the maximum light spectra.

4.5. Nebular Spectra Analysis

In the left panel of Figure 15 we plot the nebular spectra of SN 2013ge at several epochs in comparison to SN 2007gr and SN 2009jf. The late-time spectra of SN 2013ge show conspicuous features due to [OI] $\lambda\lambda$ 6300, 6364, [Ca II] $\lambda\lambda$ 7291, 7324, and Mg I λ 4571. The flux contained in the [OI] $\lambda\lambda$ 6300, 6364 feature is significantly larger than that in either [Ca II] $\lambda\lambda$ 7291, 7324 or Mg I λ 4571, with ratios of ~ 0.3 and ~ 0.12 , respectively. Notably, these ratios show very little evolution between +150 and +450 days.

The [CaII]/[OI] ratio may be an indicator of progenitor core mass, with lower values implying a larger core mass, although mixing can also play a role (Fransson & Chevalier 1989). The ratio measured in SN 2013ge is on the low end of values observed in stripped core-collapse SN, comparable to that observed in SN 2009jf.

In contrast, the ratio of Mg I/[OI] in the late-time

spectra of core-collapse SN may be sensitive to the level of stripping of the progenitor star, with a higher ratio implying more of the O-Ne-Mg layer is exposed (Foley et al. 2003). The ratio observed in SN 2013ge is small, but is particularly notable for its lack of evolution. A majority of events show a Mg I/[OI] ratio that grows with time (Hunter et al. 2009), which is expected as one probes deeper into the ejecta. For instance, in SN 2007gr (Figure 15) the Mg I/[OI] ratio grows from ~ 0.1 (similar to SN 2013ge) to ~ 1 between 150 and 450 days post maximum. This growth is *not* observed in either SN 2013ge or SN 2009jf, which may indicate that their ejecta are more thoroughly mixed.

The line profiles observed in late-time spectra of SN can offer information on the geometry of the explosion. In particular, Mazzali et al. (2005) offers a prediction for the shape of the nebular features when viewing a jetted explosion. In this study it was found that a sharp peak in the [OI] feature is consistent with viewing a jet on axis, while a spherical explosion should possess either a flat or rounded top. Taubenberger et al. (2006) used this to argue that SN 2004aw (which possesses highly peaked nebular profiles similar to SN 1998bw and SN 2002ap) was a highly aspherical explosion while SN 1994I (which possess a rounded profile) was essentially spherical. In Figure 15 we plot the [OI] $\lambda\lambda$ 6300, 6364 and [Ca II] $\lambda\lambda$ 7291, 7324 of SN 2013ge in comparison to profiles from SN 2004aw and SN 1994I. The +139d spectrum SN 2013ge appears intermediate between the rounded profiles of SN 1994I and the highly peaked profiles of SN 2004aw, while at +447 days the spectrum of SN 2013ge appears more heavily peaked, with slightly blue-shifted velocity.

4.6. The Detection of CO Emission

We identify CO-band emission from the first overtone ($\Delta v = 2$) at $\sim 2.3\mu$ in the NIR spectra of SN 2013ge. Although CO has been detected in the spectra of a

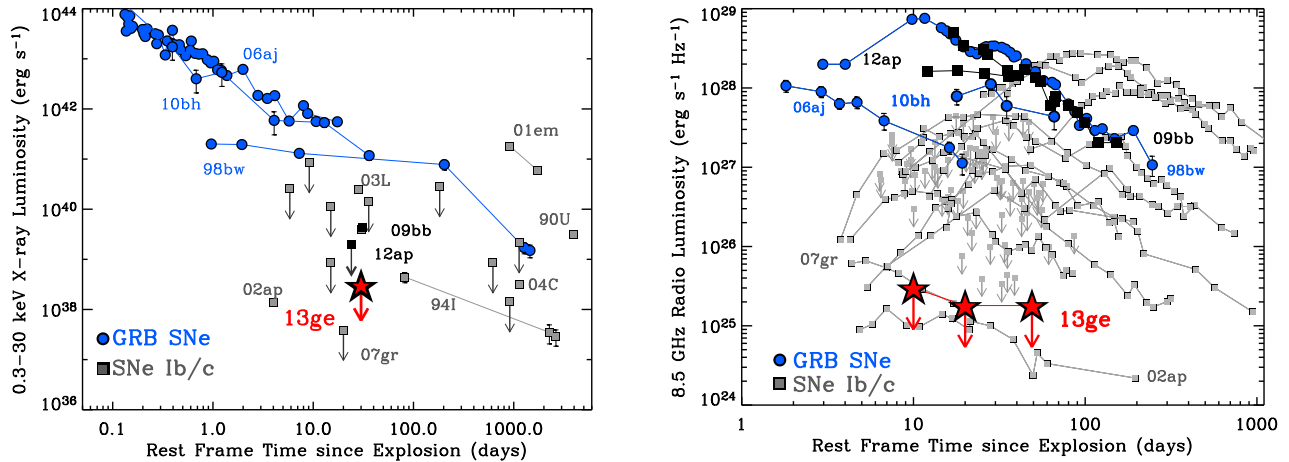


FIG. 16.— X-ray (left) and Radio (right) upper limits obtained for SN 2013ge (red stars) in comparison to other Type Ib/c SN. GRB-SNe are shown in blue, relativistic SN in black and other Type Ib/c SN in grey. The limits obtained for SN 2013ge are among the deepest obtained to date for a normal Type Ib/c SN. Only SN 2007gr and SN 2002ap have deep limits or fainter detections in either wavelength regime.

number of Type II SN, SN 2013ge is only the third Type Ib/c SN in the literature to date with molecular CO emission. Previous identifications were reported in SN 2007gr (Hunter et al. 2009) and SN 2000ew (Gerardy et al. 2002). In the right panel of Figure 15 we plot the region between 2.1μ and 2.5μ in three epochs of SN 2013ge NIR spectra (+48, +97, and +123 days). Both the CO band head and Na I are labeled.

It is evident that there is evolution of the emission profile between +48 days and +97 days. The feature dramatically narrows, an effect that, to our knowledge, has not previously been observed. The width of the emission feature observed in SN 2007gr *did not evolve* over a similar range of epochs. This behavior may be linked to different mixing properties in the ejecta of SN 2013ge and SN 2007gr, as evidenced by their nebular line ratios, above. Detailed modeling of the CO-band will be presented in Milisavljevic et al. (*in prep*).

5. LOCAL ENVIRONMENT PROPERTIES

5.1. Host Galaxy Sub-Environment

SN 2013ge exploded on the outskirts of NGC3287, an SB(s)d galaxy, approximately 51 arcseconds NE of the galaxy core. This corresponds to a normalized¹⁸ offset of 2.33. The north-east portion of NGC 3287 is characterized by a large number of blue stellar knots (see Figures 1). In our 2015 Jan 15 IMACS spectrum (445 days post maximum) the SN flux had fallen enough to reveal an unresolved knot of star formation (in the form of narrow emission lines) at the SN position.

We measured the fluxes of these emission lines at the SN explosion site using the MCMC method of Sanders et al. (2012). The measured $H\alpha$ luminosity of $\sim 1.0 \times 10^{38} \text{ erg s}^{-1}$ leads to an explosion site star formation rate of $\sim 8.0 \times 10^{-4} M_{\odot} \text{ yr}^{-1}$ (Kennicutt 1998). This value is on the low end for HII regions associated with core-collapse SN studied by Crowther (2012).

Using the PP04N2 diagnostic (Pettini & Pagel 2004), we find an explosion site metallicity for SN 2013ge of $\log(O/H) + 12 = 8.40 \pm 0.05$. This value is approxi-

mately half-solar (assuming $\log(O/H)_{\text{solar}} + 12 = 8.69$; Asplund et al. 2005) and does not deviate strongly from a metallicity measured with an SDSS spectrum taken near the galaxy core. This places the host environment metallicity of SN 2013ge in approximately the bottom 25% of the distribution measured for Type Ib and Type Ic SN and approximately the top 25% measured for Type Ic-BL in Sanders et al. (2012).

5.2. Non-Thermal Limits on Progenitor Mass-Loss Rate

As described above, we observed SN 2013ge in both the radio and X-ray bands during the main part of the optical outburst. Although we obtained only non-detections, as shown in Figure 16, these limits are among the deepest ever obtained for a Type Ib/c SN. Only the nearby ($d \sim 10 \text{ Mpc}$) Type Ic-BL SN 2002ap has intrinsically fainter emission which was *detected* in both regimes. Particularly notable, our radio observations constrain SN 2013ge to be fainter than SN 2007gr at a similar epochs.

For SN which explode into a CSM characterized by a low-density, fast, wind (as is the case for Type Ib/c SN) X-ray emission near maximum light is due to Inverse Compton (IC) up-scattering of optical photospheric emission by electrons accelerated at the SN shock. In contrast, radio emission is characterized by a synchrotron self-absorbed spectrum, created by electrons accelerated by the SN shock interacting with amplified magnetic fields (Chevalier & Fransson 2006). As such, radio and X-ray emission (or lack thereof) provide *independent* constraints on the density of the CSM surrounding the progenitor star. In this section we examine the constraints on the progenitor mass-loss rate that can be gained by both observations, as well as the implications for the progenitor system.

5.2.1. X-ray IC Limits

To model the X-ray upper limit in the context of IC up-scattering, we utilized the models of Margutti et al. (2012, 2014) which are based on the formalism of Chevalier & Fransson (2006). The luminosity of the IC signal is proportional to bolometric luminosity (L_{bol}) and additionally depends on the outer density structure of

¹⁸ Normalized by the SDSS dr10 g-band half-light radius.

the SN ejecta, the density structure of the CSM, the energy spectrum of electrons which up-scatter the optical photons, the fraction of post-shock energy in relativistic electrons (ϵ_e), and the explosion properties of the SN (ejecta mass, kinetic energy). Notably, the IC signal does not depend on the fraction of energy in magnetic fields (ϵ_B) and since $L_{IC} \propto L_{bol}$ the mass-loss rate we derive is independent of any uncertainty in the distance to the SN.

Throughout our analysis we use the bolometric light curve derived in Section 3 and assume $M_{ej} = 2.5 M_\odot$ and $E_K = 1.5 \times 10^{51}$ erg. We additionally assume that the accelerated electrons possess a power law structure with $n(\gamma) \propto \gamma^{-p}$ with $p=3$ (γ is the Lorentz factor of the electrons) and that $\epsilon_e=0.1$. These values are motivated by the study of Type Ib/c SN in the radio (e.g. Chevalier & Fransson 2006; Soderberg et al. 2006b). The outer portion of the SN ejecta is assumed to follow a steep power law of the form $\rho_{SN} \propto R^{-n}$ with $n=10$ (e.g. Matzner & McKee 1999). Finally, we consider the case where the density of the CSM can be described as a wind environment with a steady mass-loss rate \dot{M} ($\rho = \dot{M}/4\pi r^2 v_w$ where v_w is the wind velocity). Using these input parameters our X-ray limit leads to an upper limit on the progenitor mass-loss rate of $\dot{M} < 2.3 \times 10^{-5} \left(\frac{v_w}{1000 \text{ km s}^{-1}}\right) M_\odot \text{ yr}^{-1}$.

5.2.2. Radio Synchrotron Limits

As a SN shock wave ploughs through the CSM a fraction of its kinetic energy is thermalized into motion of the shock accelerated particles which gyrate in the shock amplified magnetic field and radiate synchrotron radiation. Radio emission is therefore due to the fastest moving ejecta in the SN and progenitor mass loss rate is the most fundamental property that determines the strength and evolution of radio emission. Normalizing to a constant mass loss rate and wind velocity of $\dot{M} = 10^{-5} M_\odot \text{ yr}^{-1}$ and $v_w = 1000 \text{ km s}^{-1}$, we can express the stellar wind density profile $\rho = 5 \times 10^{11} A_* r^{-2} \text{ gm/cm}^3$. For the radio spectrum characterized by synchrotron self-absorption (SSA), the peak spectral flux (F_{ν_a}) and SSA frequency (ν_a) are given by (Chevalier 1998; Kamble et al. 2014):

$$F_{\nu_a} (\text{mJy}) = 0.16 A_*^{1.36} \left(\frac{\epsilon_B}{0.1}\right)^{0.64} \left(\frac{\beta}{0.15}\right)^{4.14}$$

$$\nu_a (\text{GHz}) = 6.0 A_*^{0.64} \left(\frac{t}{10 \text{ day}}\right)^{-1.0} \left(\frac{\epsilon_B}{0.1}\right)^{0.36} \left(\frac{\beta}{0.15}\right)^{1.86}$$

where β is the shock velocity in the units of speed of light. As above, we have assumed, $n(\gamma) \propto \gamma^{-p}$ and $p = 3.0$ for the distribution of relativistic electrons.

Assuming that the shocked material is in equipartition ($\epsilon_e = \epsilon_B$) we can calculate the radio flux for various mass-loss rates both as a function of time for a given frequency and as a function of frequency for a given epoch since explosion. Each of our radio upper limits therefore places a constraint on the mass-loss rate of the progenitor system and we find that our upper limit at 9 days post explosion and at the frequency 4.8 GHz is the most constraining. This limit leads to an upper limit on the progenitor mass-loss rate of $\dot{M} < 4 \times 10^{-6} \left(\frac{v_w}{1000 \text{ km s}^{-1}}\right)$

$\left(\frac{\epsilon_B}{0.1}\right)^{-0.39} M_\odot \text{ yr}^{-1}$, where we have scaled to a fiducial value of $\epsilon_B = 0.1$. Combining this result with our X-ray limit (which does not depend on ϵ_B) we can directly constrain that $\epsilon_B > 0.01$.

5.2.3. Comparison to Other Core-Collapse SN

In Figure 17 we plot progenitor mass-loss rate versus wind speed to show how the mass-loss constraints obtained for SN 2013ge compare to those based on radio observations of 16 other stripped envelope core-collapse SN (Type IIb, Ib, Ic, and Ic-BL; see caption for references). The radio analysis only constrains \dot{M}/v_w so each SN appears as a diagonal line in this representation. The SN presented span over four orders of magnitude in \dot{M}/v_w . A horizontal line designates a wind speed of 1000 km s^{-1} , which is often taken as a fiducial value for progenitors of Type Ib/c SN. Also shown (colored squares) are regions of this phase space occupied for various classes of (single) evolved massive stars.

In interpreting the data presented in Figure 17 several caveats must be mentioned. First, we plot a single value of \dot{M}/v_w for each SN. In reality, detailed modeling of many Type Ib/c radio light curves reveals a more complex morphology, with some showing signs of density modulations or a density profiles which varies from the $\rho \propto r^{-2}$ characteristic of a steady wind (Wellons et al. 2012). Similarly the colored squares represent the locations of known local group massive stars. How the values of \dot{M} and v_w may change in the final years of a star's life is still an area study (e.g. Smith 2014), with mass-loss due to binary interaction and eruptive mass-loss events potentially creating complex CSM environments. Finally, the SN presented are those events which have both been *detected* at radio wavelengths and published in the literature, and therefore may contain some inherent biases towards brighter events.

Nevertheless, despite these caveats, several trends emerge. The Type IIb SN presented all fall at the high end of the CSM density range, with values of \dot{M}/v_w which intersect with the red/yellow supergiants, as might be expected if the progenitors have not fully lost their hydrogen envelopes¹⁹. Five Type Ib/Ic SN fall at intermediate values, and the four broad-lined Ic SN (including one GRB-SN and two relativistic SN) appear to preferentially lie in regions of low CSM density. However, it appears that SN2007gr and SN2013ge, represent examples of normal Type Ib/c SN whose progenitor CSM environments are low density, similar to those observed for the broad-lined (including engine-driven) SN.

It is possible that this trend is partially due to metallicity, as Type Ic-BL events occur preferentially in low metallicity environments (Sanders et al. 2012) and both SN 2013ge and SN 2007gr occurred in low metallicity regions of their hosts (the explosion site metallicity of SN 2007gr was $\log(\text{O}/\text{H}) + 12 = 8.5$; Modjaz et al. 2011). There is also empirical evidence that WR mass-loss rates are metallicity dependent (Crowther 2007). However, we note that the relativistic SN 2009bb and

¹⁹ Several Type IIb SN have pre explosion imaging which indicate their progenitors are Yellow Supergiants (YGSs). The mass-loss rates and wind speeds of YGSs are not well characterized in the literature, but likely fall between RSGs and LBVs on this plot.

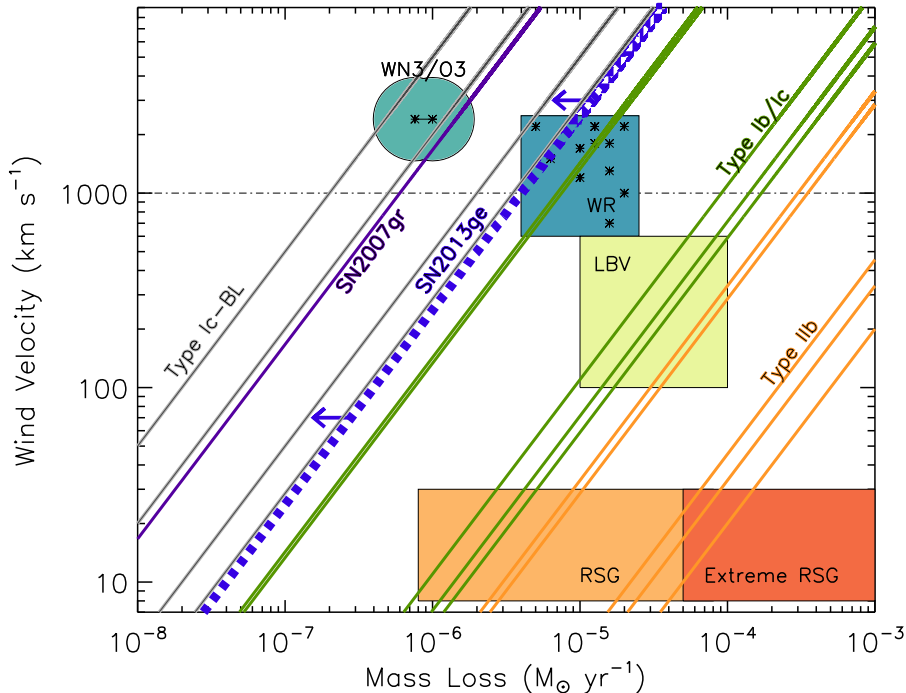


FIG. 17.— Wind Speed versus Mass-loss rate. Locations of galactic WR stars come from Crowther (2007), WN3/O3 stars from Massey et al. (2015), normal and extreme RSGs from Marshall et al. (2004), van Loon et al. (2005) and de Jager et al. (1988), and LBV wind (not outburst) properties from Smith (2014). Overplotted are measurements of progenitor mass-loss rate as a function of wind speed for SN 2013ge (this work), SN 2007gr Soderberg et al. (2010), SN 2002ap (Berger et al. 2002), SN 2006aj (Soderberg et al. 2006c), SN 2009bb (Soderberg et al. 2010), SN 2012ap (Chakraborti et al. 2015), SN 1994I (Weiler et al. 2011), SN 1990B (van Dyk et al. 1993), SN 1983N (Sramek et al. 1984), SN 2003L (Soderberg et al. 2005), SN 2008D (Soderberg et al. 2008), SN 2001ig (Ryder et al. 2004), SN 2003bg (Soderberg et al. 2006a), SN 2008ax (Roming et al. 2009), SN 2011dh (Krauss et al. 2012), and SN 2013df (Kamble et al. 2015).

SN 2012ap were both broad-lined events with low CSM densities that occurred in solar or super-solar environments (Levesque et al. 2010; Milisavljevic et al. 2015).

Intriguingly, it appears that several Type Ic-BL SN and SN 2007gr have measured values of \dot{M}/v_w which are a factor of 3 to 10 lower than any of the galactic or LMC WC and WN stars examined in Crowther (2007) (the metallicity of SN 2007gr was comparable to the LMC). However, they are consistent with the mass-loss environment inferred for the new class of WR stars recently discovered in the LMC (Massey et al. 2015). Dubbed WN3/O3, these stars are both fainter in optical bands than “normal” WN/WC stars, and (from modeling of 1 fiducial object) have inferred mass-loss rates and order of magnitude lower. While the formation mechanism of these new WR stars is not fully understood, they demonstrate that some evolved massive stars in our local group have mass-loss environments consistent with the low densities inferred from radio observations of several Type Ib/c events.

6. DISCUSSION

In this Section we discuss the observations outlined above in the context of their implications for the physical configuration of the progenitor system and explosion mechanism of SN 2013ge. From maximum light onward, the optical emission from SN 2013ge described above is fairly standard for a Type Ib/c SN. Its explosion parameters ($M_{ej}=2-3 M_{\odot}$, $E_K = 1 - 2 \times 10^{51}$ ergs) are well

within the range observed for other SN and its maximum light spectra are characterized by ions of various intermediate mass and iron peak elements at velocities of $\sim 10,000$ km s $^{-1}$.

However, the early UV and spectroscopic observations of SN 2013ge are unique. The u-band light curve shows an extra component of emission which rises on a timescale of $\sim 4-5$ days. During the rising phase of this initial peak the optical spectra are characterized by a strong blue continuum superimposed with a plethora of P Cygni features which are both rapid ($v \sim 14,000$ km s $^{-1}$) and narrow (FWHM $\lesssim 3500$ km s $^{-1}$). Below we discuss both the physical interpretation of these early spectra, possible origins for the excess UV emission, and possible progenitor scenarios which can explain both these observations and the other properties of SN 2013ge.

6.1. Physical Interpretation of the Early Spectra

When a SN shock reaches the low density outer regions of the progenitor envelope it will accelerate, leading to a high velocity gradient in the outer regions of the SN ejecta (Matzner & McKee 1999; Piro & Morozova 2014). The high velocities, rapid velocity evolution, and rapid evolution of observed ion ratios in the early spectra of SN 2013ge indicate that we are probing these outer regions. However, for a spherically symmetric explosion in which the optical depth of the ejecta decrease monotonically outward from the photosphere, a high velocity absorption minimum should be accompanied by a broad

P Cygni feature. A departure from this picture (as we see in the early spectra of SN2013ge) implies that the line formation is limited in some sense and likely requires either a modification to the geometry of the explosion or to the optical depth profile of the ejecta.

The high velocity, narrow, absorption features observed in the early spectra of SN2013ge, could be understood in terms of an asymmetric explosion in which a fraction of the ejecta was launched at high velocities along the line of sight to the observer. In this case, the width of the lines are affected by the opening angle of the ejection. After some time, this early ejection becomes transparent, revealing the underlying photosphere of the bulk explosion. Folatelli et al. (2006) evoke a similar model for the double peaked SN2005bf, which displayed both high velocity Fe II and Ca II lines and broader features (associated with the underlying photosphere) at early times. The presence of both features was understood in terms of the asymmetric explosion being close, but slightly off from the observer angle. In contrast, in SN2013ge *all* ions observed in the earliest spectra show narrow, high-velocity features; no underlying photosphere with broader components is visible. This has implications for both the ions present in such an asymmetric ejection, as well as the angle at which we observe the outflow.

Alternatively, it may be possible to recreate the spectral features in SN2013ge if the line optical depth does not decrease monotonically with radius. In this case the main line forming region at early epochs could be “detached” above the photosphere. Physically, this could be due to an actual increase in density or to a change in the ionization state of ejecta at a certain distance of above the photosphere. The latter argument was used by Tanaka et al. (2009) to explain the high velocity Ca II and Fe II lines in SN2005bf. They note that these lines coincide with high velocity H α indicating they were formed in a thin H shell which remained on the progenitor star at the time of explosion. They argue that the high electron density in this (solar abundance) H shell enhances the recombination of Ca III and Fe III (Mazzali et al. 2005; Tanaka et al. 2009), allowing narrow, high velocity Ca II and Fe II lines to be formed in the outer portions of the ejecta. In the case of SN2013ge, a plethora of high velocity ions are observed at these early epochs which would have implications for the composition of the outer layers of the progenitor star. More detailed modeling is necessary to ascertain if this is a viable explanation for the spectra of SN2013ge.

6.2. The Nature of the early UV emission

The early rising light curves of Type I SN are powered by a combination of two sources: energy deposited by the SN shock and the radioactive decay of ^{56}Ni . Excess emission can also be produced by external sources, such as the collision of the SN shock with a binary companion. We now examine the likelihood that the excess UV emission observed in the early light curve of SN2013ge is powered by each of these sources, and the implications for the explosion in each case.

6.2.1. Cooling Envelope Emission

After shock breakout, the shock heated ejecta cool, giving rise to a light curve component independent from

that powered by ^{56}Ni . During this phase, both the bolometric luminosity of the transient and the color temperature should decline with time (Nakar & Sari 2010), with the exact values depending on radius of the progenitor star, the explosion energy, the ejecta mass, and the ejecta opacity. The luminosity observed in any given optical/UV band will rise as long it is located on the Rayleigh-Jeans tail. As a result, one expects a rise in the UV/optical bands proportional to $t^{1.5}$ if the emission is powered by shock heated cooling (Piro & Nakar 2013; Nakar & Sari 2010).

In the case of SN2013ge, the observed rise time for the first u-band component is abnormally large for cooling envelope emission from a stripped progenitor star. A power-law of the form $t^{1.5}$ can be fit to the initial rise observed in the u- and w1-bands (see Figure 5; although this solution is not unique), yielding a rise time of 4–6 days from the epoch of explosion. In contrast, the cooling envelope emission from both SN2008D and SN2006aj rises in the UV/optical on timescales $\lesssim 1$ day (Soderberg et al. 2008; Campana et al. 2006). By ~ 5 days post explosion, energy from the radioactive decay of ^{56}Ni can comprise a non-negligible fraction of the total light, making it difficult to assess whether the temperature and bolometric evolution of the first component is consistent with cooling envelope emission. The u–b color evolution (tentatively) remains constant during the rising portion of the first u-band component before rapidly reddening during the decline phase (which may be consistent with the temperature passing through the observed band). However, we caution that the UV flux was depressed compared to a single blackbody during this same time period, and the rapid reddening could be due to increased line formation which depresses the UV flux.

Under the assumption that this emission is caused by shock-heated cooling then, when compared with theoretical models, the long rise time implies that SN2013ge cannot have a standard WR progenitor. In order to account for the 4–6 day rise time in the u-band, we require that the temperature remain above 10^4 K (~ 0.9 eV) *at a minimum* for this time period. In contrast, in the $5 R_{\odot}$ $15 M_{\odot}$ WR model of Nakar & Sari (2010) the temperature has already fallen below this level by $\lesssim 1$ day after explosion. Using the parameterization from Piro & Nakar (2013) for a progenitor with a hydrogen free, radiative envelope, in Figure 18 we plot the color temperature versus time for a range of progenitor radii, assuming $M_{\text{ej}} = 2\text{--}3 M_{\odot}$ and $E_{\text{K}} = 1\text{--}2 \times 10^{51}$ ergs (as derived from the bulk explosion). We see that for this progenitor envelope structure, we require a progenitor radius of at least $50 R_{\odot}$ to account for the observed u-band rise. The cooling envelope luminosity at 4 days post explosion for this model is $4 - 5 \times 10^{41}$ ergs which is compatible with the shoulder of excess emission we observe at early times.

The modest ejecta mass and extended progenitor radius derived above lead us to also consider the models of Nakar & Piro (2014) for double peaked SN. These models employ a non-standard progenitor envelope structure, in which a massive compact core is surrounded by extended low mass material. In this picture, the luminosity of the emission is mainly a function of the radius of the extended material while the time to maximum is related to the total mass in the extended envelope (with both

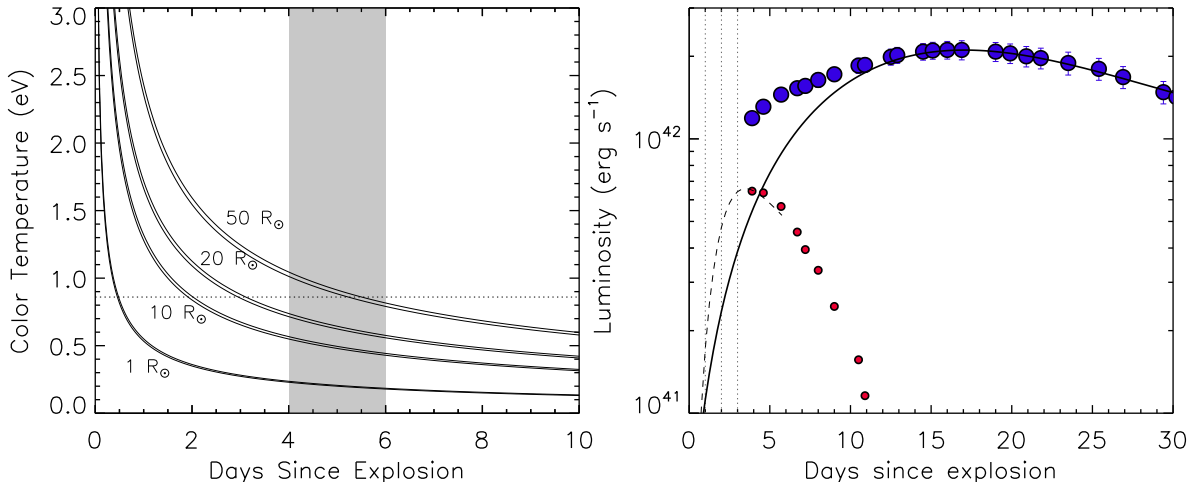


FIG. 18.— *Left*: Cooling envelope color temperature versus time since explosion for hydrogen poor progenitors with radii between $1 R_{\odot}$ and $50 R_{\odot}$. Bands for each radii assume explosion parameters of $M_{\text{ej}} = 2 - 3 M_{\odot}$ and $E_{\text{K}} = 1 - 2 \times 10^{51}$ ergs. If the early emission from SN 2013ge is due to cooling envelope emission, we require *at a minimum* that the temperature remain above 10,000 K (0.9 eV) for 4–6 days post-explosion, implying an extended progenitor. *Right*: Decomposition of the bolometric luminosity of SN 2013ge (blue) into two components. The solid black line represents our best fit ^{56}Ni decay model to the bulk explosion. Red points show the excess emission at early times above this model, and the dashed line is a fit to the rise time and luminosity of this component. Dotted lines indicate the epochs of our early spectra.

also depending on the velocity and opacity). For a peak time of 4 days, peak luminosity²⁰ of $0.6 - 1.2 \times 10^{42}$ erg s^{-1} , a characteristic velocity of $\sim 12,000$ km s^{-1} , and equations 10 and 12 of Nakar & Piro (2014) we find an extended envelope mass of $\sim 0.1 M_{\odot}$ at a radius of 15 – 25 R_{\odot} . Although less extreme than the value derived for a standard progenitor envelope structure above, this is still more extended than a typical WR progenitor star.

6.2.2. Outwardly Mixed ^{56}Ni

Alternatively, the early emission from SN 2013ge could be due to ^{56}Ni mixed outward/ejected in the explosion. This can be accomplished through either bulk asymmetries in the explosion mechanism (e.g. Scheck et al. 2006; Marek & Janka 2009; Maeda et al. 2002; Burrows et al. 2007), or through smaller scale instabilities which develop at the shock front (e.g. Kifonidis et al. 2006; Joggerst et al. 2009; Hammer et al. 2010). In this case, our rising light curve can give constraints on both the depth and radial distribution of the outwardly mixed material.

For a given light curve point, there is a degeneracy between the depth of the contributing ^{56}Ni and the explosion epoch. For deep deposits, there will be a “dark period” between the explosion epoch and the epoch of first light (Piro & Nakar 2013) before the energy diffuses outward. Our spectroscopic observations from ~ 3 days after the epoch of first light displayed high velocities and rapid velocity evolution which argue against any significant dark period for SN 2013ge. This is compatible with our first measurement of the luminosity, temperature and photospheric velocity which, using Eqn. 17 of Piro & Nakar (2013) only require the explosion epoch to be ~ 2 days prior to our first bolometric light curve

point. In this model, the lack of a significant dark period in SN 2013ge coupled with a high luminosity only ~ 4 days post explosion requires that some amount of ^{56}Ni was mixed into the very outer portions of the ejecta.

In addition, the morphology of the early bolometric light curve (see Figure 18) has implications for the radial distribution of this outwardly mixed ^{56}Ni . A radial distribution of ^{56}Ni which is monotonically decreasing should yield a smoothly rising light curve (e.g. Dessart et al. 2012). In contrast, the “shoulder” of emission as seen in SN 2013ge requires a distinct component or deposit of ^{56}Ni at shallower depths. Such a deposit could be created by a ^{56}Ni plume extending outward, or alternatively, could indicate that the SN involved an early ejection of a small amount of material followed by the slower bulk explosion. In the latter case, we can obtain an order of magnitude estimate for the ejecta mass, nickel mass, and kinetic energy of the early ejection by decomposing the bolometric light curve into two components. This is done in the right panel of Figure 18, where the solid line is our model for the bulk explosion (see Section 3) and the red points are the excess above this model at early times. Using the models of Arnett (1982) to fit the rise time and luminosity of this early component and assuming a velocity of $v_{\text{phot,p}} \sim 12,000$ km s^{-1} , we find an ejected mass of $\sim 0.04 M_{\odot}$, a ^{56}Ni mass of $\sim 0.012 M_{\odot}$, and a kinetic energy of $\sim 3 \times 10^{49}$ erg. These estimates should be taken as an order of magnitude estimate only, as they do not incorporate variations in geometry or opacity.

6.2.3. Shock Collision with a Binary Companion

Finally, we consider an external source for early UV emission in SN 2013ge: the collision of the SN ejecta with a binary companion. During such a collision, a bow shock will form, compressing and shock-heating the SN ejecta in the direction of the interaction. This heating can lead

²⁰ This is the 0.5 to 1.0 times L_{bol} at 4 days post-explosion.

extra source of UV/optical emission for several days post explosion (Kasen 2010). The observed properties of this emission depend on several parameters (e.g. binary separation, ejected mass) and is highly viewing angle dependent²¹. Using a reasonable binary population synthesis model for core collapse SN, Moriya et al. (2015) find that only $\sim 0.53\%$ of Type Ib/c SN light curves should have a detectable visible brightening due to this mechanism. As such, any detection of this collision would be rare.

Using the models of Kasen (2010), we assess whether the both the luminosity and timescale of the early emission observed in SN 2013ge can be reproduced by this mechanism. Using their Eq 22 for the luminosity of the UV/optical emission²² and the explosion parameters derived in Section 3 we find that the luminosity of the excess emission in SN 2013ge would require a binary separation of $\lesssim 10^{12}$ cm ($\sim 15 R_{\odot}$). However, reproducing the timescale of the early emission in SN 2013ge by this mechanism is challenging. The source of the UV/optical emission in this model is shock-heated cooling, analogous to the cooling envelope emission described above. Thus, in this model the rise time of 4–6 days for the first u–band component also requires that the u–band remains on the Rayleigh-Jeans tail for this time period. In contrast, none of the models presented in Kasen (2010) have rise times at these wavelengths longer than ~ 2 days. Using Eqn 15 in Kasen (2010) for the effective temperature of the emission, we find that a separation of *at least* 10^{13} cm is required to have $T_{\text{eff}} > 10^4$ K at 5 days post-explosion, inconsistent with the required separation found above. Thus, we find that (for the current set of theoretical models) our early observations of SN 2013ge are inconsistent with the collision of SN ejecta with a companion star.

6.3. The Progenitor of SN 2013ge

SN 2013ge was the explosion of a stripped massive star with a moderate ejecta mass, *weak* He features in its optical/IR spectra, a low pre-SN mass-loss rate, and a local environment metallicity of ~ 0.5 solar. Late-phase spectra also show tentative evidence for an asymmetry and/or mixing in the ejecta. However, we are left with two distinct scenarios depending on our interpretation of the early emission. Either SN 2013ge was the explosion of a star with an extended envelope or it was the result of an explosion in which a small clump of ^{56}Ni was mixed outward in the ejecta, possibly coupled to the ejection of a small amount of mass along the line of sight to the observer. We now examine the consistency and consequences of each of these progenitor models. We also emphasize that although SN 2013ge is a relatively unique object, the results presented here potentially have general implication for the progenitors of Type Ib/c SN. Without either our early spectroscopic observations or early UV coverage *SN 2013ge may not have been flagged as unusual*.

6.3.1. Extended Progenitor

If we interpret the early emission from SN 2013ge as cooling envelope emission, it implies that shock break-

out occurred from an extended surface. Our estimates for the extent of this surface range from $15 - 25 R_{\odot}$ for a low mass envelope on a compact core, to $> 50 R_{\odot}$ for a standard envelope structure. In principle, this extended surface could either be a genuinely extended progenitor envelope, or could be located within a dense optically-thick wind region surrounding the progenitor star. While some WR stars have particularly dense wind regions which extend their photospheric radii by up to a factor of 10 (Li 2007), the interpretation of SN 2013ge as the explosion of such a star is complicated by the need to reconcile with our radio observations ~ 9 days post-explosion. These observations indicate that by \sim a few $\times 10^{14}$ cm the progenitor of SN 2013ge is characterized by a *low* density wind region. Thus, unless the progenitor of SN 2013ge ejected a portion of its envelope in the final $\lesssim 1$ day prior to core-collapse, it may be better explained by the explosion of a stripped star with a low final mass-loss rate and inflated stellar envelope.

In their models examining progenitors of Type Ib/c SN from binary systems, Yoon et al. (2010) find several possible progenitors with radii inflated to $\sim 30 R_{\odot}$, low pre-SN mass-loss rates ($\dot{M} \lesssim 10^{-6} M_{\odot} \text{ yr}^{-1}$), final masses between 3–4 M_{\odot} (consistent with our derived ejecta masses), and sub-solar metallicity. However, the helium envelopes for these progenitors are predicted to be relatively large ($\sim 1.5 M_{\odot}$), and it is therefore unclear if they are consistent with the *weak* He features observed in SN 2013ge in comparison to other Type Ib SN. In particular, these low-mass, extended progenitors are predicted to be more efficient at mixing ^{56}Ni into the He-rich layers via RT-instabilities (Yoon et al. 2010; Hammer et al. 2010; Joggerst et al. 2009), which should lead to *stronger* observed He-lines. Thus, the observations of SN 2013ge may require a progenitor which differs from any presented in Yoon et al. (2010) in having an extended envelope but *low* final He mass.

Finally, we must consider if this progenitor scenario can account for the unusual early spectra observed on the rising portion of the first light curve component. In this scenario the u-band is on the Rayleigh-Jeans tail of the temperature distribution at these epochs. Yet, the ions present in these spectra are standard singly ionized species which are observed in SN spectra at much lower temperatures. It is possible that this, as well as the unusual velocity profile of the lines could be understood if there was a change in ionization state in outer portion of the ejecta, associated with the low-mass extended envelope. In this scenario, line formation would be restricted in velocity space explaining the high velocity, but narrow, absorption lines, and the ions present in the early spectra may offer insight into the composition of the progenitor envelope of SN 2013ge.

6.3.2. Early Asymmetric Ejection

If, instead, SN 2013ge resulted from the explosion of a compact progenitor, then our early bolometric light curve constrains that a distinct clump of ^{56}Ni was mixed significantly outward in the ejecta. In this case, an asymmetric ejection of a small amount of mass along the line of sight to the observer, ahead of the bulk explosion, could explain both the early emission and the unusual velocity profile in the early spectra. Intriguingly, our observed velocity ($\sim 14,000 \text{ km s}^{-1}$) and estimated mass ($\sim 0.04 M_{\odot}$)

²¹ The emission is observable mainly when viewing the shocked region on axis.

²² observed at an angle within the cone created by the interaction

for this early ejection are comparable to those observed in the high-velocity clumps in the northwest portion of the Cas A SN remnant (Fesen 2001; Laming et al. 2006). This material in the Cas A has an opening angle of ~ 45 degrees and has been argued by some to originate in the stellar core (Hwang et al. 2004; Laming et al. 2006; Milisavljevic & Fesen 2013).

Coupled with the peaked nebular emission line profiles (consistent with an asymmetric ejecta; Maeda et al. 2002; Mazzali et al. 2005) and low CSM density (similar to several jet-driven explosions), this makes it tempting to associate SN 2013ge with a highly asymmetric explosion mechanism, such as a jet or bipolar explosion from a rapidly rotating progenitor (Fryer & Heger 2000). However, the observations could also be understood if viewing one of the nickel and silicon-rich plumes of material observed in 3D simulations of mixing instabilities in neutrino driven explosions (e.g. Hammer et al. 2010). In these models, fast clumps of metal-containing material are able to penetrate through the outer layers of the ejecta, possibly leading to asymmetric variations in the ejecta velocity. Indeed, velocity variations of ~ 4000 km s^{-1} were detected in light echoes from the explosion of Cas A depending on viewing angle (Rest et al. 2011), and yet resolved imaging of the Ti in Cas A indicate that the explosion mechanism is dominated by slightly asymmetric, low-mode, convection, as opposed to a highly asymmetric/bipolar explosion mechanism (Grefenstette et al. 2014). Future detailed models could compare the abundances predicted for these metal-rich plumes with constraints from the early spectra of SN 2013ge.

In this scenario, the weak helium features observed in the spectra of SN 2013ge can also help to constrain the true He abundance of the progenitor star. In particular, they suggest a slightly different scenario than that observed in SN 2005bf, where Tanaka et al. (2009) proposed that a ^{56}Ni -rich plume penetrated only slightly into a nearly intact He-envelope. In this case, both the strength and velocity of the observed He features grew with time as more of the He envelope fell within a γ -ray optical depth of the ^{56}Ni deposit. In the case of SN 2013ge, early observations are consistent with an asymmetric ejection of ^{56}Ni which is only predicted to produce weak He features (Dessart et al. 2012). However, both the constant Mg I]/[OI] ratio and changing CO-emission profile observed in our nebular spectra favor a highly mixed ejecta for SN 2013ge at later times. Therefore, based on the lack of stronger He lines near maximum light, we favor a scenario where the progenitor of SN 2013ge was genuinely He-poor, containing only a thin layer at the time of explosion.

6.4. Comparison of the Early Emission to the Rapidly-Declining SN 2002bj

While investigating the early spectra of SN 2013ge, the only other SN spectrum we were able to identify with both a blue continuum and narrow spectroscopic features was of the very rapidly declining SN 2002bj (Poznanski et al. 2010). In Figure 19 we compare this spectrum to the -11 days spectrum of SN 2013ge. The spectrum of SN 2002bj was obtained at $+7$ days when its photospheric velocity was only ~ 4000 km s^{-1} and we have linearly blue-shifted it by 8000 km s^{-1} for comparison with SN 2013ge. We emphasize that, unlike the

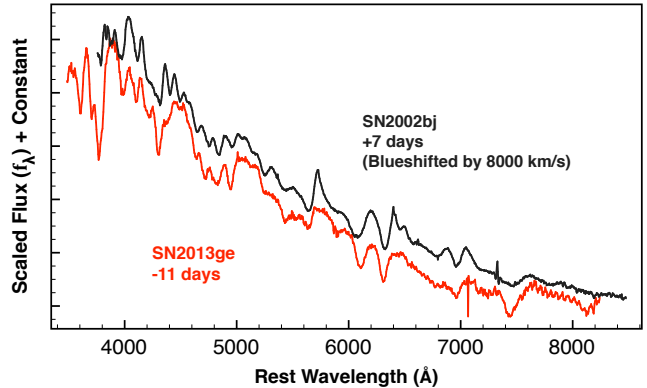


FIG. 19.— Comparison of the spectrum of the rapidly evolving SN 2002bj (Poznanski et al. 2010) to an early spectrum of SN 2013ge. The spectrum of SN 2002bj has been linearly blue-shifted by 8000 km s^{-1} .

early spectra of SN 2013ge, there is no mismatch with the width the features in the spectrum of SN 2002bj and the velocity of their absorption minima²³. However, the similarity between the spectrum of the rapidly evolving SN 2002bj and spectra obtained during the first emission component of SN 2013ge is still striking.

The nature of the explosion which produced SN 2002bj is still a mystery. The rapid light curve and unusual spectrum lead Poznanski et al. (2010) to hypothesize that it was due to the detonation of He shell on the surface of a WD. Comparing the early emission of SN 2013ge (as shown in Figure 18) to the light curve of SN 2002bj (see Figure 9) we find that the first emission component in SN 2013ge is nearly an order of magnitude fainter and also declines a factor of ~ 1.4 faster than the bolometric light curve of SN 2002bj. Even neglecting the second (main) light curve component of SN 2013ge (which is entirely lacking in SN 2002bj) the energetics of these explosions are very different. However, Figure 19 demonstrates that the ions and ionization state present in the ejecta of SN 2002bj *can also be produced during the core-collapse of a massive star*. It has already been demonstrated that massive stars may be able to produce rapidly-evolving Type I SN, either due to very low ejecta masses (Drout et al. 2013; Tauris et al. 2013) or the combination of a large progenitor radius and a lack of ejected radioactive elements (Kleiser & Kasen 2014). More detailed modeling attempting to ascertain whether SN 2002bj may be a more extreme example of the first emission component in SN 2013ge (e.g. cooling envelope emission from an extended progenitor, or a plume of outwardly mixed metal-containing material) in an explosion which lacks the second, main, light curve component powered by ^{56}Ni would be warranted.

7. SUMMARY AND CONCLUSIONS

We have presented extensive observations of the Type Ib/c SN 2013ge beginning ~ 2 days post-explosion, when the light curve is particularly sensitive to both the progenitor configuration and mixing within the ejecta. Here we summarize our main conclusions.

²³ Unfortunately, no earlier spectra of SN 2002bj is available to assess whether its spectroscopic features were similarly narrow at earlier epochs when the photospheric velocity was higher.

Early Emission: The rapid velocity evolution and rapid rise observed in the early spectra and UV light curves, respectively, indicate that our first observations probe the outer regions of the ejecta shortly after explosion. The early u-band and UV light curves show two distinct components. The first component has a rise time of $\sim 4\text{--}5$ days and is visible for the first week post explosion. This manifests itself as a “shoulder” of excess emission in the bolometric light curve with a luminosity of $\sim 6 \times 10^{41}$ ergs s^{-1} . Early spectra of the first component display a blue continuum and are unusual in possessing both high velocity ($\sim 14,000$ km s^{-1}) and narrow (~ 3500 km s^{-1}) spectroscopic features. This indicates that the line formation region is limited in some sense, possibly due to an asymmetric geometry or a change in ionization state in the very outer portions of the ejecta.

Bulk Explosion: With $M_{R,\text{peak}} = -17.5$ and $\Delta m_{15,R} = 0.4$ SN 2013ge is relatively faint and slowly evolving, but the derived ejecta mass ($2 - 3 M_{\odot}$) and kinetic energy ($1 - 2 \times 10^{51}$ ergs) are well within the distribution observed for Type Ib/c SN. Weak He I lines which fade with time are detected in early optical and NIR spectra. These lines are distinct from the conspicuous lines which are usually used to classify Type Ib SN. Near maximum light the spectra are dominated by a plethora of intermediate mass and iron peak elements. At late times, both a lack of evolution in the Mg I]/[OI] ratio and a shifting CO-emission profile may indicate mixing in the ejecta, while the peaked nebular line profile hints at a large-scale asymmetry.

Environment Properties: SN 2013ge exploded on the outskirts of a star forming galaxy. There is an unresolved HII region at the explosion site with a metallicity of ~ 0.5 solar. The radio and X-ray limits for SN 2013ge are among the deepest ever obtained for a stripped envelope SN and constrain the progenitor mass-loss rate to be $\dot{M} < 4 \times 10^{-6} M_{\odot} \text{ yr}^{-1}$ and $\epsilon_B > 0.01$.

Power Sources and Progenitors: SN 2013ge was the explosion of a stripped massive star with a moderate ejecta mass. However, we are left with two distinct progenitor scenarios depending on our interpretation of the early emission. In both cases, we find it likely that the progenitor of SN 2013ge had only thin layer of He remaining at the time of core-collapse.

1. If the early emission is due to post-shock-breakout cooling envelope emission, then its relatively long rise time ($\sim 4\text{--}6$ days) requires that the progenitor of SN 2013ge have a low mass extended envelope.
2. If the early emission is due to outwardly mixed ^{56}Ni then we require a distinct clump of ^{56}Ni mixed into the very outer portions of the ejecta. Coupled with

the early spectra this may imply an early asymmetric ejection of a small amount of mass.

More detailed modeling beyond the scope of this work will be necessary to fully distinguish between or rule out one of these two progenitor scenarios. In particular, detailed models are necessary to ascertain whether either scenario can actually reproduce the plethora of high velocity and narrow features observed in the early spectra, with the cooling envelope model facing the additional challenge of explaining the depressed UV flux at early epochs. We note that if the epoch of first light is earlier than that derived in Section 3 from power law fits to the early UV light curves, then the cooling envelope/extended progenitor scenario would be put under additional tension, or ruled out entirely. In contrast, the model of an outflow/high velocity clump could be naturally extended to explain an increase in the rate of rise in the UV light curves at some point after the epoch of first light. Finally, we find that current theoretical models for the collision of a SN shock with a binary companion cannot reproduce both the luminosity and timescale of the early emission observed in SN 2013ge.

Rapidly-Evolving SN 2002bj: The early spectra of SN 2013ge show remarkable similarity to the spectrum of the rapidly-evolving SN 2002bj, demonstrating that the ions and ionization state present in the ejecta of SN 2002bj can also be produced by the core collapse of a massive star.

M. R. D. thanks L. Z. Kelley, D. Kasen, and E. Ramirez-Ruiz for useful discussions regarding this manuscript. We thank N. Morrell for obtaining some of the observations reported here. M. R. D. is supported in part by the NSF Graduate Research Fellowship. M.L.G.s position in the supernova research group at U.C. Berkeley is supported by Gary and Cynthia Bengier and NSF grant AST-1211916.

This paper includes data gathered with the 6.5 m Magellan Telescopes located at Las Campanas Observatory, Chile. Some observations reported here were obtained at the MMT observatory, a joint facility of the Smithsonian Institution and the University of Arizona. This paper uses data taken with the MODS spectrographs built with funding from NSF grant AST-9987045 and the NSF Telescope System Instrumentation Program (TSIP), with additional funds from the Ohio Board of Regents and the Ohio State University Office of Research.

Facilities: *Swift*-UVOT, Magellan:Baade (IMACS, FIRE), Magellan:Clay (LDSS3), MMT (Blue Channel spectrograph, Hectospec, MMTCam), LBT (MODS), CAO, FLWO (FAST, KeplerCam), Chandra, VLA, Lick:Shane (Kast), MDM (OSMOS)

REFERENCES

- Allington-Smith, J., Breare, M., Ellis, R., et al. 1994, PASP, 106, 983
- Arcavi, I., Gal-Yam, A., Yaron, O., et al. 2011, ApJ, 742, L18
- Arnett, W. D. 1982, ApJ, 253, 785
- Asplund, M., Grevesse, N., & Sauval, A. J. 2005, in *Astronomical Society of the Pacific Conference Series*, Vol. 336, *Cosmic Abundances as Records of Stellar Evolution and Nucleosynthesis*, ed. T. G. Barnes, III & F. N. Bash, 25
- Begelman, M. C., & Sarazin, C. L. 1986, ApJ, 302, L59
- Benetti, S., Turatto, M., Valenti, S., et al. 2011, MNRAS, 411, 2726
- Berger, E., Kulkarni, S. R., & Chevalier, R. A. 2002, ApJ, 577, L5
- Bersten, M. C., Benvenuto, O. G., Nomoto, K., et al. 2012, ApJ, 757, 31
- Blondin, S., Matheson, T., Kirshner, R. P., et al. 2012, AJ, 143, 126
- Branch, D., Jeffery, D. J., Young, T. R., & Baron, E. 2006, PASP, 118, 791
- Branch, D., Benetti, S., Kasen, D., et al. 2002, ApJ, 566, 1005

- Breeveld, A. A., Landsman, W., Holland, S. T., et al. 2011, in American Institute of Physics Conference Series, Vol. 1358, American Institute of Physics Conference Series, ed. J. E. McEnery, J. L. Racusin, & N. Gehrels, 373–376
- Brown, P. J., Holland, S. T., Immler, S., et al. 2009, *AJ*, 137, 4517
- Burrows, A., Dessart, L., Livne, E., Ott, C. D., & Murphy, J. 2007, *ApJ*, 664, 416
- Campana, S., Mangano, V., Blustin, A. J., et al. 2006, *Nature*, 442, 1008
- Cao, Y., Kasliwal, M. M., Arcavi, I., et al. 2013, *ApJ*, 775, L7
- Chakraborti, S., Soderberg, A., Chomiuk, L., et al. 2015, *ApJ*, 805, 187
- Chen, J., Wang, X., Ganeshalingam, M., et al. 2014, *ApJ*, 790, 120
- Chevalier, R. A. 1998, *ApJ*, 499, 810
- Chevalier, R. A., & Fransson, C. 2006, *ApJ*, 651, 381
- Corsi, a., Ofek, E. O., Gal-Yam, a., et al. 2012, *ApJ*, 747, L5
- Crowther, P. A. 2007, *ARA&A*, 45, 177
- Crowther, P. a. 2012, *MNRAS*, 1943, 1927
- de Jager, C., Nieuwenhuijzen, H., & van der Hucht, K. A. 1988, *A&AS*, 72, 259
- Dessart, L., Hillier, D. J., Li, C., & Woosley, S. 2012, *MNRAS*, 424, 2139
- Dressler, A., Hare, T., Bigelow, B. C., & Osip, D. J. 2006, in Society of Photo-Optical Instrumentation Engineers (SPIE) Conference Series, Vol. 6269, Society of Photo-Optical Instrumentation Engineers (SPIE) Conference Series
- Drout, M. R., Soderberg, A. M., Gal-Yam, A., et al. 2011, *ApJ*, 741, 97
- Drout, M. R., Soderberg, A. M., Mazzali, P. A., et al. 2013, *ApJ*, 774, 58
- Elmhamdi, A., Danziger, I. J., Branch, D., & Leibundgut, B. 2007, in American Institute of Physics Conference Series, Vol. 924, The Multicolored Landscape of Compact Objects and Their Explosive Origins, ed. T. di Salvo, G. L. Israel, L. Piersant, L. Burderi, G. Matt, A. Tornambe, & M. T. Menna, 277–284
- Fabricant, D., Cheimets, P., Caldwell, N., & Geary, J. 1998, *PASP*, 110, 79
- Fabricant, D., Fata, R., Roll, J., et al. 2005, *PASP*, 117, 1411
- Fesen, R. A. 2001, *ApJS*, 133, 161
- Filippenko, A. V. 1997, *ARA&A*
- Filippenko, A. V., Barth, A. J., Matheson, T., et al. 1995, *ApJ*, 450, L11
- Folatelli, G., Contreras, C., Phillips, M. M., et al. 2006, *ApJ*, 641, 1039
- Foley, R. J., Papenkova, M. S., Swift, B. J., et al. 2003, *PASP*, 115, 1220
- Foley, R. J., Challis, P. J., Chornock, R., et al. 2013, *ApJ*, 767, 57
- Fransson, C., & Chevalier, R. A. 1989, *ApJ*, 343, 323
- Fremling, C., Sollerman, J., Taddia, F., et al. 2014, *A&A*, 565, A114
- Fryer, C. L., & Heger, A. 2000, *ApJ*, 541, 1033
- Gehrels, N., Chincarini, G., Giommi, P., et al. 2004, *ApJ*, 611, 1005
- Gerardy, C. L., Fesen, R. A., Nomoto, K., et al. 2002, *PASJ*, 54, 905
- Gorbikov, E., Gal-Yam, A., Ofek, E. O., et al. 2014, *MNRAS*, 443, 671
- Grefenstette, B. W., Harrison, F. A., Boggs, S. E., et al. 2014, *Nature*, 506, 339
- Hachinger, S., Mazzali, P. A., Taubenberger, S., et al. 2012, *MNRAS*, 422, 70
- Hachinger, S., Mazzali, P. a., Taubenberger, S., et al. 2012, *MNRAS*, 422, 70
- Hammer, N. J., Janka, H.-T., & Müller, E. 2010, *ApJ*, 714, 1371
- Hicken, M., Challis, P., Kirshner, R. P., et al. 2012, *ApJS*, 200, 12
- Hsiao, E. Y., Marion, G. H., Phillips, M. M., et al. 2013, *ApJ*, 766, 72
- Hunter, D. J., Valenti, S., Kotak, R., et al. 2009, *A&A*, 508, 371
- Hwang, U., Laming, J. M., Badenes, C., et al. 2004, *ApJ*, 615, L117
- Joggerst, C. C., Woosley, S. E., & Heger, A. 2009, *ApJ*, 693, 1780
- Kalberla, P. M. W., Burton, W. B., Hartmann, D., et al. 2005, *A&A*, 440, 775
- Kamble, A., Soderberg, A. M., Chomiuk, L., et al. 2014, *ApJ*, 797, 2
- Kamble, A., Margutti, R., Soderberg, A. M., et al. 2015, *ArXiv e-prints*
- Kasen, D. 2010, *ApJ*, 708, 1025
- Kennicutt, R. C. 1998, *ARA&A*, 36, 189
- Kifonidis, K., Plewa, T., Scheck, L., Janka, H.-T., & Müller, E. 2006, *A&A*, 453, 661
- Kleiser, I. K. W., & Kasen, D. 2014, *MNRAS*, 438, 318
- Krauss, M. I., Soderberg, A. M., Chomiuk, L., et al. 2012, *ApJ*, 750, L40
- Laming, J. M., Hwang, U., Radics, B., Lekli, G., & Takács, E. 2006, *ApJ*, 644, 260
- Landolt, A. U. 1992, *AJ*, 104, 340
- Levesque, E. M., Soderberg, a. M., Foley, R. J., et al. 2010, *ApJ*, 709, L26
- Li, L.-X. 2007, *MNRAS*, 375, 240
- Lucy, L. B. 1991, *ApJ*, 383, 308
- Maeda, K., Mazzali, P. A., Deng, J., et al. 2003, *ApJ*, 593, 931
- Maeda, K., Nakamura, T., Nomoto, K., et al. 2002, *ApJ*, 565, 405
- Marek, A., & Janka, H.-T. 2009, *ApJ*, 694, 664
- Margutti, R., Parrent, J., Kamble, A., et al. 2014, *ApJ*, 790, 52
- Margutti, R., Soderberg, A. M., Chomiuk, L., et al. 2012, *ApJ*, 751, 134
- Margutti, R., Guidorzi, C., Lazzati, D., et al. 2015, *ApJ*, 805, 159
- Marshall, J. R., van Loon, J. T., Matsuura, M., et al. 2004, *MNRAS*, 355, 1348
- Martini, P., Stoll, R., Derwent, M. A., et al. 2011, *PASP*, 123, 187
- Massey, P., Neugent, K. F., Morrell, N., & John Hillier, D. 2015, in IAU Symposium, Vol. 307, IAU Symposium, 64–69
- Matheson, T., Kirshner, R. P., Challis, P., et al. 2008, *AJ*, 135, 1598
- Matzner, C. D., & McKee, C. F. 1999, *ApJ*, 510, 379
- Mazzali, P. A., Kawabata, K. S., Maeda, K., et al. 2005, *Science*, 308, 1284
- Milislavljevic, D., & Fesen, R. A. 2013, *ApJ*, 772, 134
- Milislavljevic, D., Fesen, R., Pickering, T., et al. 2013, *The Astronomer's Telegram*, 5142, 1
- Milislavljevic, D., Margutti, R., Parrent, J. T., et al. 2015, *ApJ*, 799, 51
- Millard, J., Branch, D., Baron, E., et al. 1999, *ApJ*, 527, 746
- Miller, J. S., & Stone, R. P. S. 1993, *Lick Observatory Technical Reports*, Vol. 66 (Santa Cruz, CA: Lick Obs.)
- Modjaz, M., Kewley, L., Bloom, J. S., et al. 2011, *ApJ*, 731, L4
- Modjaz, M., Li, W., Butler, N., et al. 2009a, *ApJ*, 702, 226
- , 2009b, *ApJ*, 702, 226
- Moriya, T. J., Liu, Z.-W., & Izzard, R. G. 2015, *MNRAS*, 450, 3264
- Mould, J. R., Huchra, J. P., Freedman, W. L., et al. 2000, *ApJ*, 529, 786
- Nakar, E. 2015, *ArXiv e-prints*
- Nakar, E., & Piro, A. L. 2014, *ApJ*, 788, 193
- Nakar, E., & Sari, R. 2010, *ApJ*, 725, 904
- Nugent, P. E., Sullivan, M., Cenko, S. B., et al. 2011, *Nature*, 480, 344
- Parrent, J., Friesen, B., & Parthasarathy, M. 2014, *Ap&SS*, 351, 1
- Parrent, J., Branch, D., Troxel, M. A., et al. 2007, *PASP*, 119, 135
- Parrent, J. T. 2014, *ArXiv e-prints*
- Parrent, J. T., Milislavljevic, D., Soderberg, A. M., & Parthasarathy, M. 2015, *ArXiv e-prints*
- Pastorello, a., Kasliwal, M. M., Crockett, R. M., et al. 2008, *MNRAS*, 389, 955
- Pettini, M., & Pagel, B. E. J. 2004, *MNRAS*, 348, L59
- Phillips, M. M., Li, W., Frieman, J. A., et al. 2007, *PASP*, 119, 360
- Piro, A. L., & Morozova, V. S. 2014, *ApJ*, 792, L11
- Piro, A. L., & Nakar, E. 2013, *ApJ*, 769, 67
- Podsiadlowski, P., Joss, P. C., & Hsu, J. J. L. 1992, *ApJ*, 391, 246
- Pogge, R. W., Atwood, B., Brewer, D. F., et al. 2010, in Society of Photo-Optical Instrumentation Engineers (SPIE) Conference Series, Vol. 7735, Society of Photo-Optical Instrumentation Engineers (SPIE) Conference Series, 0
- Poznanski, D., Prochaska, J. X., & Bloom, J. S. 2012, *MNRAS*, 426, 1465
- Poznanski, D., Chornock, R., Nugent, P. E., et al. 2010, *Science*, 327, 58
- Rabinak, I., & Waxman, E. 2011, *ApJ*, 728, 63
- Rest, A., Foley, R. J., Sinnott, B., et al. 2011, *ApJ*, 732, 3

TABLE 1
UVOT PHOTOMETRY

UT Date	MJD	<i>uvw</i> 2 (err) mag	<i>uvm</i> 2 (err) mag	<i>uvw</i> 1 (err) mag	<i>u</i> (err) mag	<i>b</i> (err) mag	<i>v</i> (err) mag
2013 Nov 11	56607.0	16.66 (0.08)	15.34 (0.06)
2013 Nov 11	56607.8	17.32 (0.07)	17.37 (0.06)	16.20 (0.06)	15.03 (0.04)	15.79 (0.04)	15.69 (0.06)
2013 Nov 12	56608.7	17.21 (0.07)	17.36 (0.07)	16.18 (0.06)	14.94 (0.04)	15.61 (0.04)	15.54 (0.06)
2013 Nov 13	56609.8	17.29 (0.07)	17.40 (0.07)	16.11 (0.05)	14.87 (0.04)	15.56 (0.04)	15.32 (0.05)
2013 Nov 14	56610.8	17.37 (0.08)	17.46 (0.10)	16.25 (0.06)	15.03 (0.05)	15.55 (0.04)	15.20 (0.05)
2013 Nov 15	56611.3	17.53 (0.08)	17.50 (0.08)	16.44 (0.07)	15.05 (0.05)	15.46 (0.04)	15.26 (0.05)
2013 Nov 16	56612.1	17.54 (0.08)	17.70 (0.08)	16.55 (0.07)	15.21 (0.05)	15.43 (0.04)	15.15 (0.05)
2013 Nov 17	56613.1	17.57 (0.08)	17.93 (0.12)	16.69 (0.07)	15.26 (0.05)	15.46 (0.04)	15.11 (0.05)
2013 Nov 18	56614.6	17.72 (0.08)	...	16.79 (0.07)	15.30 (0.05)	15.47 (0.04)	14.98 (0.05)
2013 Nov 19	56615.1	17.76 (0.08)	18.07 (0.09)	16.80 (0.07)	15.39 (0.05)	15.42 (0.04)	14.94 (0.04)
2013 Nov 20	56616.7	17.86 (0.09)	17.92 (0.09)	16.82 (0.07)	15.39 (0.05)	15.51 (0.04)	14.95 (0.05)
2013 Nov 21	56617.1	17.75 (0.08)	17.94 (0.09)	16.85 (0.07)	15.42 (0.05)	15.36 (0.04)	14.83 (0.04)
2013 Nov 22	56618.6	16.83 (0.06)	15.46 (0.04)	15.39 (0.04)	14.78 (0.06)
2013 Nov 23	56619.2	16.98 (0.06)	15.47 (0.04)	15.38 (0.04)	14.87 (0.08)
2013 Nov 24	56620.1	17.15 (0.07)	15.61 (0.04)	15.54 (0.04)	14.76 (0.07)
2013 Nov 27	56623.1	17.25 (0.08)	15.84 (0.05)	15.55 (0.04)	14.81 (0.04)
2013 Nov 29	56625.9	17.40 (0.08)	16.16 (0.05)	15.77 (0.05)	14.93 (0.06)
2013 Dec 1	56627.7	17.39 (0.07)	16.49 (0.05)	16.07 (0.04)	15.00 (0.05)
2013 Dec 3	56629.5	17.38 (0.07)	16.70 (0.05)	16.10 (0.04)	15.03 (0.06)
2013 Dec 5	56631.1	17.61 (0.08)	16.77 (0.06)	16.30 (0.05)	15.24 (0.06)
2013 Dec 7	56633.5	17.74 (0.10)	16.91 (0.07)	16.46 (0.06)	15.36 (0.06)
2013 Dec 9	56635.2	17.90 (0.10)	17.08 (0.07)	16.62 (0.06)	15.48 (0.07)

- Richmond, M. W., van Dyk, S. D., Ho, W., et al. 1996, *AJ*, 111, 327
- Roming, P. W. A., Kennedy, T. E., Mason, K. O., et al. 2005, *Space Sci. Rev.*, 120, 95
- Roming, P. W. A., Pritchard, T. A., Brown, P. J., et al. 2009, *ApJ*, 704, L118
- Ryder, S. D., Sadler, E. M., Subrahmanyam, R., et al. 2004, *MNRAS*, 349, 1093
- Sahu, D. K., Gurugubelli, U. K., Anupama, G. C., & Nomoto, K. 2011, *MNRAS*, 413, 2583
- Sanders, N. E., Soderberg, a. M., Levesque, E. M., et al. 2012, *ApJ*, 758, 132
- Scheck, L., Kifonidis, K., Janka, H.-T., & Müller, E. 2006, *A&A*, 457, 963
- Schlafly, E. F., & Finkbeiner, D. P. 2011, *ApJ*, 737, 103
- Schmidt, G. D., Weymann, R. J., & Foltz, C. B. 1989, *PASP*, 101, 713
- Silverman, J. M., Foley, R. J., Filippenko, A. V., et al. 2012, *MNRAS*, 425, 1789
- Simcoe, R. A., Burgasser, A. J., Schechter, P. L., et al. 2013, *PASP*, 125, 270
- Smith, J. A., Tucker, D. L., Kent, S., et al. 2002, *AJ*, 123, 2121
- Smith, N. 2014, *ARA&A*, 52, 487
- Soderberg, a. M., Brunthaler, a., Nakar, E., Chevalier, R. a., & Bietenholz, M. F. 2010, *ApJ*, 725, 922
- Soderberg, A. M., Chevalier, R. A., Kulkarni, S. R., & Frail, D. A. 2006a, *ApJ*, 651, 1005
- Soderberg, A. M., Kulkarni, S. R., Berger, E., et al. 2005, *ApJ*, 621, 908
- Soderberg, A. M., Nakar, E., Berger, E., & Kulkarni, S. R. 2006b, *ApJ*, 638, 930
- Soderberg, A. M., Kulkarni, S. R., Nakar, E., et al. 2006c, *Nature*, 442, 1014
- Soderberg, a. M., Berger, E., Page, K. L., et al. 2008, *Nature*, 453, 469
- Soderberg, A. M., Chakraborti, S., Pignata, G., et al. 2010, *Nature*, 463, 513
- Speziali, R., Di Paola, A., Giallongo, E., et al. 2008, in *Society of Photo-Optical Instrumentation Engineers (SPIE) Conference Series*, Vol. 7014, *Society of Photo-Optical Instrumentation Engineers (SPIE) Conference Series*, 4
- Sramek, R. A., Panagia, N., & Weiler, K. W. 1984, *ApJ*, 285, L59
- Tanaka, M., Kawabata, K. S., Maeda, K., et al. 2009, *ApJ*, 699, 1119
- Taubenberger, S., Pastorello, A., Mazzali, P. a., et al. 2006, *MNRAS*, 371, 1459
- Tauris, T. M., Langer, N., Moriya, T. J., et al. 2013, *ApJ*, 778, L23
- Thomas, R. C., Nugent, P. E., & Meza, J. C. 2011, *PASP*, 123, 237
- Valenti, S., Elias-Rosa, N., Taubenberger, S., et al. 2008, *ApJ*, 673, L155
- Valenti, S., Fraser, M., Benetti, S., et al. 2011, *MNRAS*, 416, 3138
- van Dyk, S. D., Sramek, R. A., Weiler, K. W., & Panagia, N. 1993, *ApJ*, 409, 162
- van Dyk, S. D., Zheng, W., Fox, O. D., et al. 2014, *AJ*, 147, 37
- van Loon, J. T., Cioni, M.-R. L., Zijlstra, A. A., & Loup, C. 2005, *A&A*, 438, 273
- Weiler, K. W., Panagia, N., Stockdale, C., et al. 2011, *ApJ*, 740, 79
- Wellons, S., Soderberg, A. M., & Chevalier, R. A. 2012, *ApJ*, 752, 17
- Wheeler, J. C., Harkness, R. P., Khokhlov, A. M., & Hoefflich, P. 1995, *Phys. Rep.*, 256, 211
- Wheeler, J. C., Johnson, V., & Clocchiatti, A. 2015, *MNRAS*, 450, 1295
- Wheeler, J. C., & Levreault, R. 1985, *ApJ*, 294, L17
- Wheeler, J. C., Barker, E., Benjamin, R., et al. 1993, *ApJ*, 417, L71
- Woosley, S., & Weaver, T. 1995, *ApJSS*, 101, 181
- Yoon, S.-C., Woosley, S. E., & Langer, N. 2010, *ApJ*, 725, 940

TABLE 2
CAO PHOTOMETRY

UT Date	MJD	<i>B</i> (err) mag	<i>V</i> (err) mag	<i>R</i> (err) mag	<i>I</i> (err) mag
2013 Nov 12	56608.5	...	15.62 (0.08)	15.67 (0.12)	15.43 (0.21)
2013 Nov 22	56618.5	15.51 (0.07)	14.88 (0.04)	14.70 (0.04)	14.41 (0.04)
2013 Nov 23	56619.5	15.46 (0.08)	14.80 (0.04)	14.55 (0.04)	14.33 (0.04)
2013 Nov 24	56620.5	15.53 (0.06)	14.83 (0.05)	14.51 (0.03)	14.30 (0.03)
2013 Nov 25	56621.5	15.64 (0.13)	14.87 (0.04)	14.68 (0.06)	14.35 (0.07)
2013 Nov 26	56622.5	15.63 (0.06)	14.82 (0.03)	14.66 (0.05)	14.33 (0.04)
2013 Nov 28	56624.5	15.83 (0.09)	14.94 (0.04)	14.58 (0.03)	14.25 (0.03)
2013 Nov 29	56625.5	15.93 (0.11)	14.96 (0.07)	14.58 (0.03)	14.27 (0.05)
2013 Dec 5	56631.5	...	15.41 (0.13)	14.80 (0.09)	14.42 (0.14)
2013 Dec 11	56637.5	...	15.60 (0.20)	14.98 (0.14)	14.56 (0.17)
2013 Dec 12	56638.5	...	15.85 (0.08)	15.09 (0.04)	14.63 (0.07)
2013 Dec 14	56640.5	...	15.87 (0.08)	15.10 (0.05)	14.64 (0.07)

TABLE 3
FLWO PHOTOMETRY

UT Date	MJD	B (err) mag	V (err) mag	r' (err) mag	i' (err) mag
2013 Dec 7	56633.4	16.70 (0.02)	15.54 (0.02)	15.15 (0.03)	15.06 (0.03)
2013 Dec 7	56633.5	16.71 (0.03)	15.55 (0.03)	15.15 (0.05)	15.08 (0.04)
2013 Dec 8	56634.4	16.70 (0.02)	15.54 (0.02)	15.14 (0.01)	15.04 (0.01)
2013 Dec 14	56640.3	17.16 (0.02)	15.93 (0.02)	15.47 (0.02)	15.35 (0.03)
2013 Dec 23	56649.5	17.36 (0.03)	16.27 (0.01)	15.85 (0.01)	15.72 (0.01)
2013 Dec 24	56650.5	17.57 (0.03)	16.35 (0.02)	15.91 (0.03)	15.78 (0.03)
2013 Dec 26	56652.5	17.54 (0.02)	16.36 (0.01)	15.93 (0.01)	15.84 (0.02)
2013 Dec 27	56653.5	17.53 (0.02)	16.40 (0.01)	15.95 (0.01)	15.85 (0.01)
2013 Dec 28	56654.5	17.62 (0.02)	...	16.02 (0.03)	15.91 (0.03)
2013 Dec 29	56655.5	15.92 (0.05)
2013 Dec 30	56656.3	17.52 (0.02)	16.42 (0.01)	15.96 (0.01)	15.84 (0.01)
2014 Jan 1	56658.5	17.65 (0.02)	16.48 (0.02)	16.08 (0.02)	...
2014 Jan 2	56659.5	...	16.49 (0.01)	16.07 (0.01)	15.99 (0.01)
2014 Jan 3	56660.3	17.71 (0.04)	16.54 (0.03)	16.13 (0.04)	15.93 (0.02)
2014 Jan 6	56663.5	17.71 (0.02)	16.58 (0.05)	16.19 (0.05)	16.10 (0.06)
2014 Jan 9	56666.4	17.76 (0.03)	16.64 (0.02)	...	16.19 (0.03)
2014 Jan 11	56668.3	17.76 (0.02)	16.65 (0.01)	16.29 (0.02)	16.23 (0.02)
2014 Jan 12	56669.5	17.80 (0.03)	16.70 (0.03)	16.30 (0.03)	16.27 (0.04)
2014 Jan 13	56670.5	17.78 (0.02)	16.70 (0.03)	16.34 (0.02)	16.31 (0.03)
2014 Jan 14	56671.4	17.83 (0.03)	16.73 (0.04)	16.38 (0.04)	16.32 (0.04)
2014 Jan 15	56672.5	...	16.70 (0.01)	16.32 (0.01)	16.29 (0.01)
2014 Jan 16	56673.5	17.88 (0.04)	16.78 (0.03)	16.44 (0.05)	...
2014 Jan 17	56674.4	...	16.69 (0.01)	16.27 (0.02)	16.35 (0.01)
2014 Jan 18	56675.4	17.85 (0.03)	16.77 (0.02)	16.44 (0.03)	16.44 (0.03)
2014 Jan 19	56676.5	...	16.82 (0.03)	...	16.50 (0.04)
2014 Jan 20	56677.4	17.92 (0.04)	16.85 (0.03)	16.49 (0.03)	16.48 (0.03)
2014 Jan 21	56678.4	17.89 (0.02)	...	16.50 (0.02)	16.49 (0.02)
2014 Jan 23	56680.4	17.86 (0.02)	16.87 (0.02)	16.53 (0.03)	16.55 (0.03)
2014 Jan 26	56683.5	17.92 (0.02)	16.91 (0.03)	16.59 (0.03)	16.61 (0.02)
2014 Jan 28	56685.4	17.90 (0.02)	16.95 (0.02)	16.60 (0.03)	16.63 (0.03)
2014 Feb 3	56691.3	17.97 (0.02)	17.00 (0.02)	16.70 (0.02)	16.77 (0.03)
2014 Feb 6	56694.4	...	17.05 (0.03)
2014 Feb 9	56697.4	18.08 (0.02)	17.13 (0.02)	16.81 (0.02)	16.89 (0.02)
2014 Feb 12	56700.3	18.14 (0.02)	17.20 (0.02)	16.87 (0.02)	16.96 (0.02)
2014 Feb 13	56701.4	18.16 (0.03)	17.21 (0.03)	16.89 (0.03)	17.01 (0.04)
2014 Feb 14	56702.3	18.20 (0.03)	17.21 (0.03)	16.90 (0.02)	17.03 (0.03)
2014 Feb 15	56703.5	18.18 (0.04)
2014 Feb 18	56706.4	18.20 (0.02)	17.28 (0.03)	16.97 (0.03)	17.09 (0.04)
2014 Feb 20	56708.5	18.11 (0.02)	17.31 (0.02)	17.02 (0.02)	17.15 (0.03)
2014 Feb 25	56713.2	18.19 (0.03)	17.34 (0.04)	17.05 (0.03)	17.15 (0.02)
2014 Feb 25	56713.3	18.30 (0.03)	17.42 (0.05)	17.07 (0.03)	...
2014 Feb 27	56715.2	18.24 (0.03)	17.35 (0.02)	17.07 (0.02)	17.22 (0.02)
2014 Feb 27	56715.5	18.28 (0.03)	17.39 (0.02)	17.11 (0.02)	17.25 (0.03)
2014 Mar 5	56721.5	17.08 (0.02)	17.24 (0.02)
2014 Mar 6	56722.3	18.38 (0.03)	17.54 (0.04)	17.19 (0.04)	17.35 (0.03)
2014 Mar 14	56730.5	18.50 (0.04)	17.67 (0.03)	17.29 (0.02)	17.60 (0.04)
2014 Mar 15	56731.4	...	17.63 (0.03)
2014 Mar 17	56733.3	18.63 (0.04)	17.77 (0.03)	17.38 (0.03)	17.62 (0.03)
2014 Mar 19	56735.3	18.50 (0.05)	17.77 (0.07)	17.33 (0.07)	17.61 (0.13)
2014 Mar 25	56741.3	18.68 (0.03)	17.88 (0.04)	17.50 (0.04)	17.71 (0.03)
2014 Mar 30	56746.3	18.73 (0.10)	17.75 (0.05)
2014 Apr 2	56749.3	18.64 (0.03)	18.00 (0.02)	17.58 (0.02)	17.71 (0.02)
2014 Apr 7	56754.3	18.64 (0.03)	18.00 (0.02)	17.57 (0.02)	17.91 (0.03)
2014 Apr 30	56777.2
2014 May 3	56780.2	19.46 (0.03)	18.70 (0.02)	18.12 (0.03)	18.39 (0.03)

TABLE 4
MMTCAM, LBT, AND IMACS PHOTOMETRY

UT Date	MJD	r (err) mag	i (err) mag	z (err) mag	Instrument
2013 Nov 19	56615.5	15.01 (0.03)	14.98 (0.04)	15.04 (0.05)	MMTCam
2014 Apr 1	56748.1	17.59 (0.05)	17.85 (0.02)	...	MMTCam
2014 Apr 4	56751.3	17.69 (0.03)	17.91 (0.02)	17.04 (0.01)	MMTCam
2014 May 21	56798.2	18.41 (0.02)	18.71 (0.03)	...	MMTCam
2014 June 7	56815.1	18.71 (0.04)	18.92 (0.01)	...	MMTCam
2014 Oct 22	56952.1	20.48 (0.05)	20.96 (0.02)	...	LBT
2014 Nov 20	56981.5	21.18 (0.03)	21.62 (0.03)	...	MMTCam
2014 Dec 18	57009.3	21.36 (0.02)	IMACS
2015 Jan 15	57037.3	21.65 (0.03)	IMACS
2015 Feb 10	57063.4	22.13 (0.06)	22.58 (0.04)	...	MMTCam
2015 Apr 16	57128.1	> 22.3	> 22.4	...	MMTCam

TABLE 5
VLA OBSERVATIONS

UT Date	MJD	Frequency GHz	F mJy
2013 Nov 16	56612.8	4.8	<45.6
...	...	7.1	<42.0
2013 Nov 26	56622.4	4.8	< 36.0
...	...	7.1	< 30.9
2014 Jan 4	56661.3	4.8	< 36.0
...	...	7.1	< 29.3

TABLE 6
OPTICAL AND INFRARED SPECTROSCOPY

UT Date	MJD	Telescope	Instrument ^a
2013 Nov 9	56605	MMT	BC
2013 Nov 10	56606	MMT	BC ^b
2013 Nov 10	56606	MMT	BC
2013 Nov 11	56607	MMT	BC
2013 Nov 20	56616	Magellan-Baade	FIRE
2013 Nov 21	56617	MMT	Hectospec
2013 Nov 29	56625	MMT	Hectospec
2013 Nov 30	56626	Magellan-Baade	FIRE
2013 Dec 6	56632	Tillinghast 60-in	FAST
2013 Dec 7	56633	Tillinghast 60-in	FAST
2013 Dec 9	56634	Magellan-Baade	FIRE
2013 Dec 10	56636	Tillinghast 60-in	FAST
2013 Dec 13	56639	MDM 2.4-m	OSMOS
2013 Dec 24	56650	MMT	BC
2013 Dec 27	56653	MMT	BC
2013 Dec 28	56654	MMT	BC
2013 Dec 31	56657	Magellan-Clay	LDSS-3
2014 Jan 1	56658	Magellan-Baade	FIRE
2014 Jan 3	56660	Tillinghast 60-in	FAST
2014 Jan 6	56663	Tillinghast 60-in	FAST
2014 Jan 7	56664	Tillinghast 60-in	FAST
2014 Jan 9	56666	Tillinghast 60-in	FAST
2014 Jan 9	56666	Magellan-Baade	FIRE
2014 Jan 25	56682	Shane 3-m	Kast
2014 Jan 28	56685	Tillinghast 60-in	FAST
2014 Jan 30	56687	Tillinghast 60-in	FAST
2014 Feb 2	56690	Tillinghast 60-in	FAST
2014 Feb 2	56690	Magellan-Baade	FIRE
2014 Feb 3	56691	Magellan-Baade	IMACS
2014 Feb 26	56714	Tillinghast 60-in	FAST
2014 Feb 27	56715	Magellan-Baade	FIRE
2014 Mar 4	56720	Tillinghast 60-in	FAST
2014 Mar 6	56722	MMT	BC
2014 Mar 7	56723	Tillinghast 60-in	FAST
2014 Mar 25	56741	Magellan-Baade	FIRE
2014 Apr 28	56775	MMT	BC
2014 Oct 23	56953	LBT	MODS
2015 Jan 15	57037	Magellan-Baade	IMACS

^a Instrument References: FAST spectrograph (Fabricant et al. 1998) on the FLWO 60-inch Tillinghast telescope; Blue Channel (BC) spectrograph (Schmidt et al. 1989) on the 6.5 MMT; hectospec multi-fiber spectrograph (Fabricant et al. 2005) on the MMT; Low Dispersion Survey Spectrograph-3 (LDSS-3; Allington-Smith et al. 1994) on Magellan-Clay, the Inamori-Magellan Areal Camera & Spectrograph (IMACS; Dressler et al. 2006) on Magellan-Baade, OSMOS on the MDM 2.4-m (Martini et al. 2011), the Kast spectrograph (Miller & Stone 1993) on Shane 3-m at Lick Observatory, and the Multi-Object Double Spectrograph (MODS; Pogge et al. 2010) mounted on the 2×8.4 -m LBT; Folded-port InfraRed Echellette spectrograph (FIRE; Simcoe et al. 2013) on Magellan-Baade

^b Observation with 1200 grating.

TABLE 7
BASIC PHOTOMETRIC PROPERTIES

Band	T _{max} (MJD)	m _{obs,max} (mag)	M _{abs,max} (mag)	Δm_{15} (mag)	Neb. Decline Rate ^a (mag day ⁻¹)
<i>w2</i>	56608.7 (1.1)	18.51 (0.06)	-13.36 (0.05)	>0.65	...
<i>m2</i>	56607.7 (1.0)	18.40 (0.05)	-13.47 (0.05)	>0.70	...
<i>w1</i>	56608.8 (1.0)	17.18 (0.04)	-14.69 (0.04)	1.23 (0.08)	...
<i>u</i>	56609.4 (1.1)	15.56 (0.04)	-16.31 (0.04)	1.16 (0.05)	...
<i>B</i>	56615.7 (1.5)	14.93 (0.03)	-16.94 (0.03)	1.11 (0.05)	0.0119 (0.0004)
<i>V</i>	56618.6 (1.5)	14.52 (0.05)	-17.35 (0.05)	0.74 (0.11)	0.0156 (0.0003)
<i>R</i>	56621.1 (1.5)	14.55 (0.03)	-17.32 (0.03)	0.44 (0.05)	0.0155 (0.0003)
<i>I</i>	56623.1 (1.5)	14.54 (0.03)	-17.33 (0.03)	0.38 (0.06)	0.0198 (0.0004)

^a measured from a linear fit between +60 and +120 days.